Climate Dynamics
https://doi.org/10.1007/s00382-020-05244-z

Interannual variability of East African rainfall: role of seasonal transitions of the low-level cross-equatorial flow

Edward K. Vizy[1] · **Kerry H. Cook**[1]

Received: 18 December 2019 / Accepted: 10 April 2020

Abstract
During boreal spring and fall, the low-level cross-equatorial flow along the East African coast weakens and reverses. These transition periods are embedded within the East African rainy seasons—the spring long rains and the fall short rains. ERAI, ERA5, JRA-55, and MERRA2 atmospheric reanalyses and CHIRPS2 and ARC2 rainfall observations are examined to improve our understanding of how the transition periods vary on interannual timescales, and how these variations are related to regional rainfall. Transition period length is positively correlated with spring and fall East African rainfall regionally. Variations in transition period length are associated with the seasonal development and variability of three low-level circulation features, namely, the South Indian Convergence Zone, the Mascarene High over the South Indian Ocean, and the Arabian High over the Arabian Sea. In addition to affecting the low-level moisture transport and convergence over East Africa, these circulation features interact to influence the start and end dates that define the transition period. Composites are constructed and analyzed for different transition period types based on length, start date, and end date to distinguish differences among event types as well as seasonal differences. Air–sea coupling over the western Indian Ocean is stronger for the spring transition than for the fall, modifying precipitation through variations in specific humidity. In the fall transition period, rainfall variations are primarily controlled by circulation variations. These results have implications for climate change prediction over East Africa, for example, as the Indian Ocean warms.

Keywords East African rainfall · Kenya · Rainfall variability · Mascarene high · Indian Ocean · Ethiopia · Tanzania · Low-level jet · Somali jet · Long rains · Short rains

1 Introduction

The atmospheric Somali or Findlater jet is a narrow, low-level circulation feature that flows northward along the East African coast from May through September (Findlater 1969; Krishnamurti and Bhalme 1976). During boreal winter, an equally strong northeasterly low-level cross equatorial flow associated with the Asian winter monsoon flows into the Southern Hemisphere along the East African coast. Both of these cross-equatorial flows are directed, in part, by the East African topography, and they both carry large amounts of moisture into the summer hemisphere. Being among the region's dominant low-level circulation features, they also help determine East African precipitation distributions. In particular, the boreal spring long rain and the fall short rain seasons that characterize equatorial East Africa (~ 10° S–5° N) precipitation occur when the large-scale cross-equatorial flow is in transition between its summer and winter configurations.

The purpose of this paper is to understand how interannual variations in the transitioning of the large-scale, cross-equatorial circulation along the East African coast influence the interannual variability of East African rainfall. Background on this cross equatorial flow and East African rainfall is provided in Sect. 2. Section 3 introduces the atmospheric reanalyses and rainfall datasets utilized in this study, and discusses analysis methods. Results are presented in Sect. 4, while findings are summarized and conclusions drawn in Sect. 5.

✉ Edward K. Vizy
ned@jsg.utexas.edu

[1] Department of Geological Sciences, Jackson School of Geosciences, The University of Texas at Austin, Austin, TX 78712, USA

Published online: 16 April 2020

2 Background

The annual cycle of rainfall over East Africa from southern Ethiopia/Somalia to northern Tanzania is generally bimodal (Ogallo 1993; Camberlin and Philippon 2002; Yang et al. 2015; Nicholson 2017), consisting of wet seasons during the boreal spring and boreal fall that are known as the 'long rains' and 'short rains', respectively. The long rains typically commence in late February/early March with rainfall intensity peaking around the beginning of April and declining in May. For the short rains, rainfall starts in mid to late October, peaks in November, and declines in late November/early December. Compared to the short rains, the long rains typically produce heavier and more total rainfall (Griffiths 1972; Nicholson 1996), and tend to be less variable than the short rains (Nicholson 2017). The seasonal evolution of the long and short rains is not a smooth transition. Instead, it is characterized by a series of abrupt 'jumps' in the rainfall activity (Riddle and Cook 2008), suggesting a strong connection with the seasonal evolution of the regional circulation features.

Of particular relevance for East African rainfall variability are three low-level circulation features over the western Indian Ocean. The first is the cross-equatorial low-level jet (a.k.a. the Findlater or Somali Jet during the boreal summer). This jet is associated with persistent cross-equatorial flow during the solsticial seasons, providing inflow into the summer Indian monsoon during the boreal summer (Findlater 1969), and reversing direction during the boreal winter associated with outflow from the Asian winter monsoon. This jet is forced by differential heating over the Indian Ocean basin and adjacent continents with East African topography playing an important role in confining this low-level jet along the coast (Krishnamurti et al. 1976; Rodwell and Hoskins 1995). The seasonal development of this low-level jet is strongly related to the seasonality of rainfall over East Africa with the abrupt "jumps" in the location of the heaviest rainfall found to be associated with the different stages of jet development (Riddle and Cook 2008). For example, the boreal spring/summer jet undergoes a two stage setup with the cross-equatorial meridional southerly branch developing during the spring, while the zonal westerly/southwesterly branch develops during the early summer associated with the development of the Indian summer monsoon (Ramage 1971; Pant and Kumar 1997; Webster et al. 1998; Riddle and Cook 2008).

The second feature is the Mascarene High, which is located over the South Indian Ocean. While the Mascarene High persists through the year, it is stronger and centered farther south and east (~ 83° E, 32° S) during austral summer, and weaker and farther northwest (~ 59° E, 29° S) during austral winter. Anticyclonic low-level flow associated with this high influences the low-level trade winds and SSTAs over the southwestern Indian Ocean (Anyamba and Ogallo 1985; Manatsa et al. 2014), and variations in this feature can affect low-level convergence and moisture transport from the southwestern Indian Ocean into East Africa (Manatsa et al. 2014; Manatsa and Behera 2014; Morioka et al. 2015).

The last feature is the Arabian anticyclone, or Arabian High. This high pressure system is strongest during the boreal winter. It is centered over the Arabian Peninsula, with anticyclonic low-level flow extending over the Arabian Sea (Lashkari et al. 2016). The center shifts southeastward over the Arabian Sea in March before weakening and dissipating by the end of April/early May. The high is absent during the boreal summer, but reforms over the Arabian Peninsula in October. The position and intensity of this anticyclone can influence the low-level circulation over the Arabian Sea and the Horn of Africa by affecting the meridional low-level height gradients and trade winds (Sun et al. 1999; Camberlin and Okoola 2003; Ayugi et al. 2018).

Given East Africa's propensity to experience rainfall extremes, both devastating floods such as the 2018 event (FEWSNET 2018) and droughts, and the importance of rainfall for agricultural purposes, there has been considerable effort to understand rainfall variability over this region. As highlighted by Cook and Vizy (2019), a number of recent studies evaluate long-term East African long rains trends, usually for the 1980–2010 time period, and find negative trends averaged across large areas (Lyon and DeWitt 2012; Funk et al. 2015; Maidment et al. 2015). In particular, there is a tendency for drying during the 2000–2009 period, although the exact location of the drying varies in different studies (Ongoma and Chen 2017; Funk et al. 2015). For the short rains, studies suggest the opposite of the long rains with an increase rainfall in areas over East Africa (Clarke et al. 2003; Funk et al. 2005, 2008, 2013; Ummenhofer et al. 2009; Lyon and Dewitt 2012; Liebmann et al. 2014; Maidment et al. 2015; Ayugi et al. 2016). The decrease in the long rains has been linked with changes in the zonal SST gradients between Indonesia and the central equatorial Pacific (Liebmann et al. 2014; Yang et al. 2015), while SSTAs in the Indian Ocean may be influential for the change in the short rains (Funk et al. 2008; Owiti et al. 2008; Maidment et al. 2015; Ummenhofer et al. 2018). On shorter timescales, SSTAs, particularly in the Indian Ocean, have also been found to influence East African long and short rains variability (Owiti et al. 2008; Ogwang et al. 2015; Ummenhofer et al. 2018; Liu et al. 2020), although Atlantic variability (Camberlin and Okoola 2003; Williams et al. 2012) and ENSO (Mutai et al. 1998; Indeje et al. 2001; Nicholson and Selato 2000; Black et al. 2003; Manatsa et al. 2014; Ogwang et al. 2015) can also be influential.

Other factors can effect East African rainfall variability. For example, the position, intensity, and seasonality of both the Mascarene and Arabian High pressure systems over the Indian Ocean can influence the low-level northeasterly and southeasterly trade wind regimes that, in turn, modify the advection of moisture from the Indian Ocean and its convergence over East Africa (Sun et al. 1999; Camberlin and Okoola 2003; Hastenrath et al. 2011; Nicholson 2016; Ayugi et al. 2018). The Mascarene high is known to vary with the Southern Annular Mode (Fauchereau et al. 2003; Hermes and Reason 2005; Wen-Jing and Zi-Nu 2014; Manatsa et al. 2014, 2016; Morioka et al. 2015; Ogwang et al. 2015).

3 Datasets and methodology

3.1 Datasets

Multiple atmospheric reanalyses and observational rainfall datasets are analyzed to support confidence in the findings. Each dataset utilized is described briefly below.

Four state-of-the-art atmospheric reanalyses are selected for analysis of the cross-equatorial flow, the regional circulation, and surface conditions. They are:

- ECMWF ERA-Interim (ERAI; Dee et al. 2011)—ERAI provides ~ 0.75° resolution global 6-hourly output of atmospheric fields from 1979 to 2018. 6-hourly values are averaged to formulate daily means.
- ECMWF ERA5 reanalysis (ERA5; C3S 2017)—ERA5 is the 5th generation product available from ECMWF providing global 0.25° resolution hourly gridded output of surface and atmospheric fields from 1979—2018. Here, hourly data is averaged to formulate daily mean values for this study.
- NASA Modern-Era Retrospective analysis for Research and Applications, Version 2 (MERRA2; Gelaro et al. 2017)—MERRA2 provides global 3-hourly estimates of upper-air fields and hourly estimates of some surface fields on 0.625° longitude × 0.5° latitude resolution grid from 1980 to present. 3-hourly upper air and hourly surface fields are used to form daily mean values.
- Japan Meteorological Agency's 55-year reanalysis (JRA-55; Kobayashi et al. 2015)—JRA-55 provides global 1.25° resolution 6-hourly upper air and surface fields from 1958 to present. We only analyze data from 1979 to 2018 to directly compare to the other atmospheric reanalyses mentioned above. 6-hourly values are used to formulate daily mean values.

Two rainfall datasets are evaluated. These datasets are selected because both have high spatial resolutions to account for the inhomogeneity of rainfall over the complex terrain of East Africa, and sufficiently long records of daily rainfall information (from the early 1980s to present) that are needed to evaluate interannual variations of the transition periods. The precipitation datasets are:

- Climate Hazards group InfraRed Precipitation with Stations Version 2 (CHIRPS2; Funk et al. 2015)—this product provides 0.1° resolution daily rainfall estimates over land from 1981 to present. CHIRPS2 blends 0.05° resolution satellite imagery with in-situ measurements to produce a gridded daily values.
- NOAA Climate Prediction Center African Rainfall Climatology Version 2 (ARC2; Novella and Thiaw 2013)—ARC2 provides 0.1° resolution daily rainfall estimates over Africa from 1983 to present. The ARC2 algorithm blends EUMETSAT 3-hourly geostationary satellite IR information with quality-controlled Global Telecommunication System gauge observations to produce gridded daily estimates.

3.2 Methodology

To relate interannual variations in the fall and spring transitions of the cross-equatorial low-level flow to East African rainfall variability, the circulation transition periods need to be defined quantitatively. First, two daily time series of the 925-hPa meridional wind speed averaged between 40° E–50° E on the equator are formulated from 1979 to 2018 in each reanalysis. This location (925 hPa and 40° E–50° E) is where there is a peak in the cross-equatorial meridional flow in the climatological annual mean. One-time series is the raw data, and the other is detrended and smoothed. Linear detrending is used to remove multi-decadal time scales and a 30-day running mean smoothing is applied to remove sub-seasonal variations to focus on interannual time scales. As an example for one spring season (1979), Fig. 1a shows the raw (blue) and smoothed (red) time series.

These two time series are used together to define transition-period (boreal spring and fall) start and end dates (and, thereby, transition period lengths) for each year of the 40 years analyzed. These dates are defined as the day on which the averaged 925-hPa meridional wind speed near the equator reaches a threshold "weak" value in the detrended and smoothed time series which denotes the transition period. This threshold value is determined through the following process:

- First, start and end dates in the raw time series for each year are defined as the first and last dates, respectively, in a given season when there is a reversal in the sign of the averaged meridional wind. These dates are indicated by the blue arrows in the example shown in Fig. 1a.

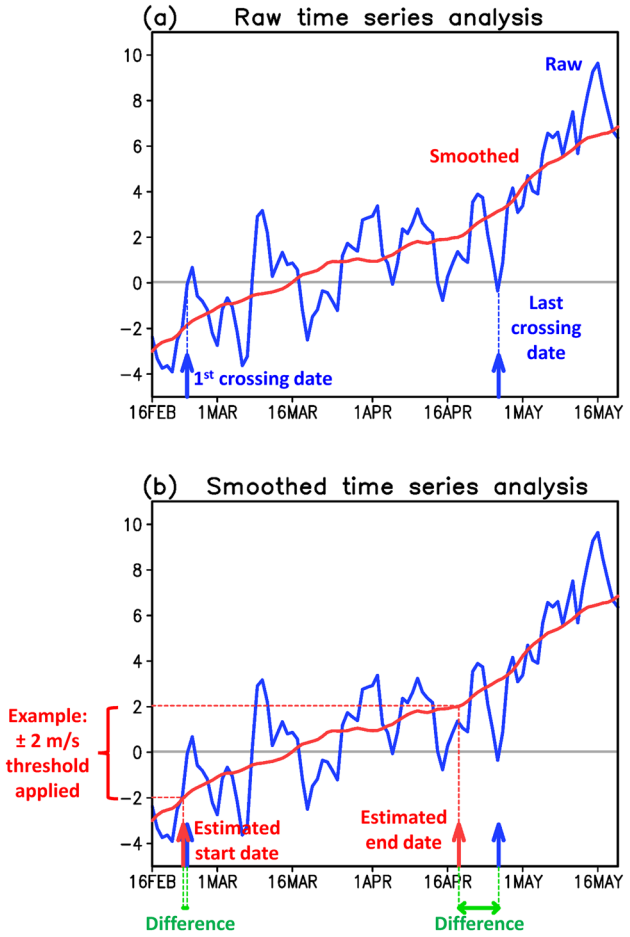

Fig. 1 Example raw (blue) and detrended and smoothed (red) daily time series for the boreal spring of 1979 from ERA5 to illustrate the methodology for defining the transition periods. **a** Demonstration of how the first and last crossing dates are identified in the raw time series. **b** Demonstration of how a meridional wind threshold is applied to estimate start and end dates for the transition period from the detrended and smoothed time series, and how differences from the raw time series crossing dates are determined. The vertical axes are meridional wind speed in m s^{-1}

- The next step is to assume a reasonable, but necessarily arbitrary, initial estimate for the threshold value. Figure 1b shows an example in which a ± 2 m s^{-1} threshold is applied. This threshold is then used to estimate start and end dates for each season, each year, and each reanalysis from the detrended and smoothed time series (red arrows in Fig. 1b). Differences from the dates selected from the raw time series (first step) are calculated (green in Fig. 1b) and summed to produce a total difference for the 40-year analysis period.
- The previous step is repeated with other estimates for the threshold wind speed (ranging between ± 2.5 m s^{-1}) to find the speed that produces the smallest total 40-year difference in dates for each reanalysis.
- The threshold wind speed estimates associated with the smallest total difference in each reanalysis are selected and averaged to define one threshold "weak" wind speed. The threshold values selected by this process are ± 1.61 m s^{-1} from ERA5, ± 1.59 m s^{-1} from ERAI, ± 1.75 m s^{-1} from JRA-55, and ± 1.65 m s^{-1} MERRA2, and the average is ± 1.65 m s^{-1}.

With the threshold wind value chosen, start and end dates are determined using the detrended and smoothed time series, defining transition periods for each year and each reanalysis. In the analysis, data are first averaged over each year's transition period in each reanalysis, and averaged together to form the transition period climatology (Sect. 4.1). Then compositing (detailed in Sect. 4.3) is used to characterize types of transition periods, and the statistical significance of differences between the types is calculated using the Student's *t* test. Confidence in the results is also supported by using multiple datasets to test for robustness.

4 Results

4.1 Climatological analysis of the spring and fall transition periods

Before evaluating interannual variability, we establish a climatological perspective of how the spring and fall transitions periods evolve. Table 1 lists the 1979–2018 average boreal spring and fall start date, end date, and transition period lengths and their standard deviations from the four reanalyses and the multi-reanalysis mean using the method described in Sect. 3.2. In the multi-reanalysis mean, the boreal spring transition period is 32 days in length starting on March 3rd and ending on April 3rd. The transition period length ranges from 30 days in MERRA2, which has a later start date compared to the other reanalyses, to 35 days in JRA-55, which has a later end date. The transition period length standard deviations vary from 8.44 days in MERRA2 to 9.98 days in ERAI. Start and end date standard deviations are lower (~7 days) than standard deviations for the transition period length, and vary among the reanalyses by about 1 day for the start date and 2 days for the end date.

The boreal fall transition period is shorter than the spring transition period, lasting 25 days with a start date on November 9th and end date on December 3rd. The range of the reanalyses is also smaller for the length (23–27 days), start date (November 6–11), and end date (December 2–5) compared to the spring, as are the standard deviations of length, start date, and end date.

Figure 2 shows the ERAI climatological 925-hPa low-level geopotential heights and winds at different stages of the spring and fall transition periods. Different stages are shown

Table 1 The 1979–2018 average boreal spring and fall transition period length, start, and end dates from various atmospheric reanalyses and their multi-reanalysis average

Reanalysis	Period	Avg Length (Days)	Avg. length St. Dev (Days)	Avg Start (Date)	Avg. start St. Dev (Days)	Avg End (Date)	Avg. end St. Dev (Days)
ERAI	Spring	33.15	9.98	MAR 1	7.51	APR 3	6.55
ERA5	Spring	30.33	9.22	FEB 28	7.64	MAR 30	6.66
JRA-55	Spring	34.90	9.37	MAR 5	6.37	APR 8	8.14
MERRA2	Spring	30.10	8.44	MAR 7	6.44	APR 5	7.14
AVERAGE	Spring	32.12	9.25	MAR 3	6.99	APR 3	7.12
ERAI	Fall	25.90	7.28	NOV 8	4.72	DEC 3	6.87
ERA5	Fall	24.83	7.66	NOV 11	5.55	DEC 5	7.14
JRA-55	Fall	26.83	8.34	NOV 6	5.70	DEC 2	7.04
MERRA2	Fall	23.51	8.10	NOV 9	6.69	DEC 2	6.61
AVERAGE	Fall	25.27	7.85	NOV 9	5.67	DEC 3	6.92

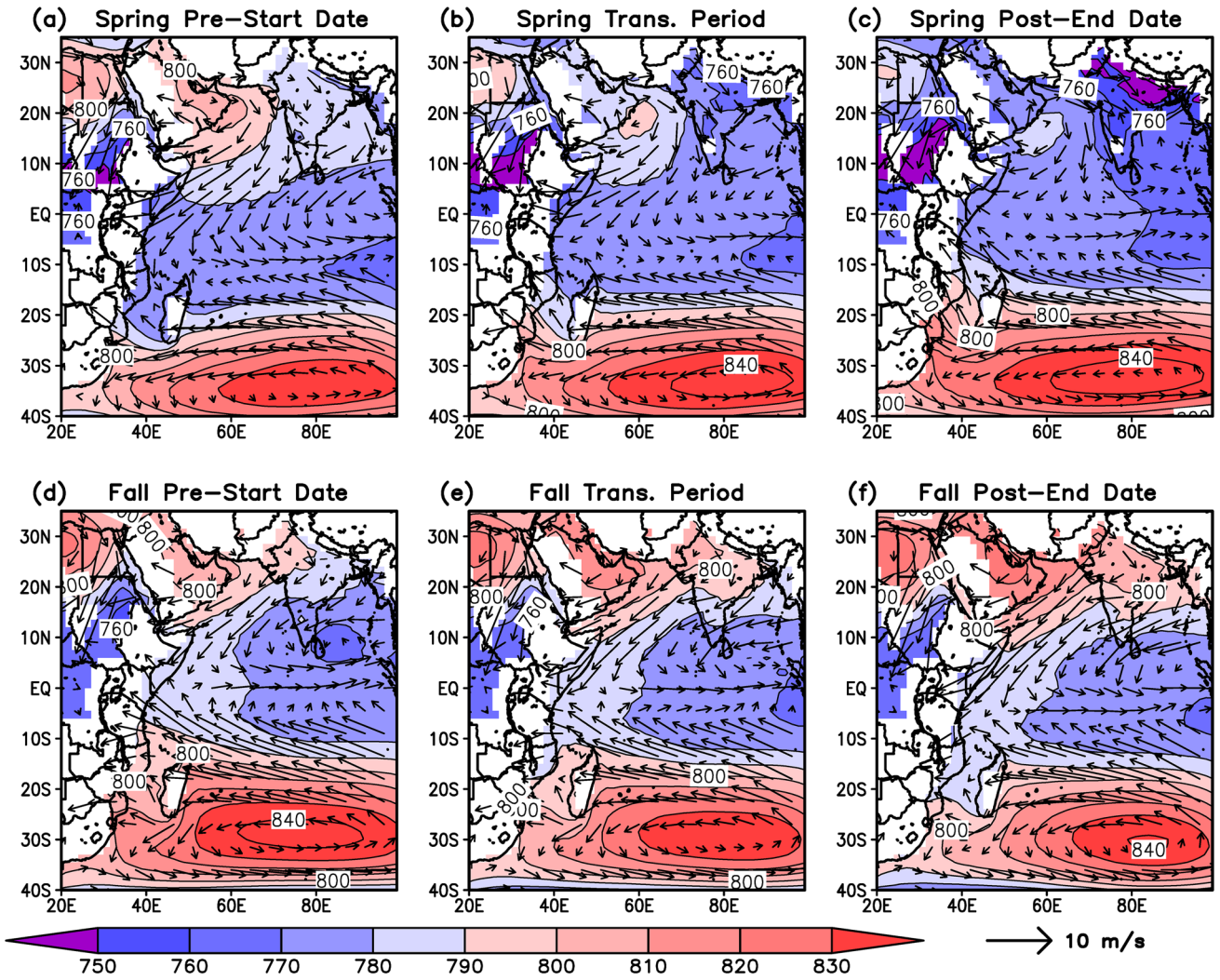

Fig. 2 ERAI 1979–2018 climatological 925 hPa geopotential heights (shading; m) and wind (vectors; m s^{-1}) averaged over **a** the 10-days prior to the defined spring transition period start date, **b** the spring transition period, and **c** the 10-days after the defined spring transition period end date. **d**–**f** are the same as **a**–**c**, respectively, but for the fall transition period

in Fig. 2 to highlight changes in the low-level circulation associated with the development from start and end of the transition period. The other reanalyses (not shown) closely resemble the results from ERAI. For 10 days prior to the climatological start of the spring transition period (Fig. 2a), strong northeasterly flow extends from India and the Arabian Sea across the equator to about 10° S in association with ridging over the Arabian Sea and Arabian Peninsula. While a component of this flow is directed onshore over East Africa, most crosses the equator. A dominant circulation feature in the Southern Hemisphere is the Mascarene High, centered near 35° S and 85° E. Circulation around this feature is anticyclonic, but its influence on the low-level flow between 5° S–15° S and west of Madagascar is relatively weak at this time as the Mascarene High is transitioning from its weakest intensity and southeastern-most positioning during the late austral summer. The low-level circulation west of Madagascar and over southern Africa is more strongly influenced by the South Indian Convergence Zone (SICZ) and Mozambique Channel Trough (MCT), both of which are also gradually weakening from their austral summer peak intensities (Cook 2000; Munday and Washington 2017; Barimalala et al. 2018). In Fig. 2a, note the low-level cyclonic flow over the Mozambique Channel, and that the geopotential heights between 15° S–22° S are lower than those east of Madagascar at comparable latitudes.

After the start of the spring transition period (Fig. 2b), there is a breakdown of the SICZ/MCT over the Mozambique Channel and an intensification of the Mascarene High. East of Madagascar, the low-level meridional height gradient between 10° S–20° S is stronger than in the pre-start period (Fig. 2a), and the easterly flow is stronger. With the breakdown of the SICZ/MCT between the Mozambique Coast and 50° E, the meridional height gradient changes considerably, and is associated with the development of easterly/southeasterly flow into the eastern Africa coast between the equator and 17° S. North of the equator the low-level ridging over the Arabian Sea and Arabian Peninsula weakens, and the low-level northeasterly flow is weaker and directed more easterly. Thus, the low-level flow is predominantly easterly from Tanzania to Somalia, enhancing the onshore flow of moisture that supports the development of convection.

Immediately following the end of the spring transition period (Fig. 2c), stronger low-level ridging of high pressure occurs over the southwestern Indian Ocean along the eastern African coast, while the low-level high over the Arabian Sea continues to weaken. These changes are associated with the development and intensification of southerly cross-equatorial flow. The flow remains anticyclonic over the Arabian Sea, indicating that the Indian summer monsoon has not yet developed.

A similar evolution in the low-level circulation occurs during the fall. Prior to the climatological start date (Fig. 2d), the Mascarene High is strong over the southwestern Indian Ocean and there is strong ridging between the coast and Madagascar accompanied by strong, southeasterly low-level flow into Kenya and Tanzania. North of the equator, low-level ridging over the northern Arabian Sea and Arabian Peninsula is developing, but the associated low-level northeasterly flow does not reach the equator. During the fall transition period (Fig. 2e), the Mascarene High begins to weaken and shift southeastward, and ridging over the Mozambique Channel also begins to weaken along with the low-level southeasterly flow into Kenya and Tanzania. North of the equator, ridging has intensified over the Arabian Sea/Arabian Peninsula, and low-level northeasterly flow extends to the equator. After the transition period ends (Fig. 2f), ridging continues to weaken over the southwestern Indian Ocean. Northeasterly flow, associated with the further intensification of ridging over the Arabian Peninsula and Arabian Sea, now extends along the coast and into the southern hemisphere.

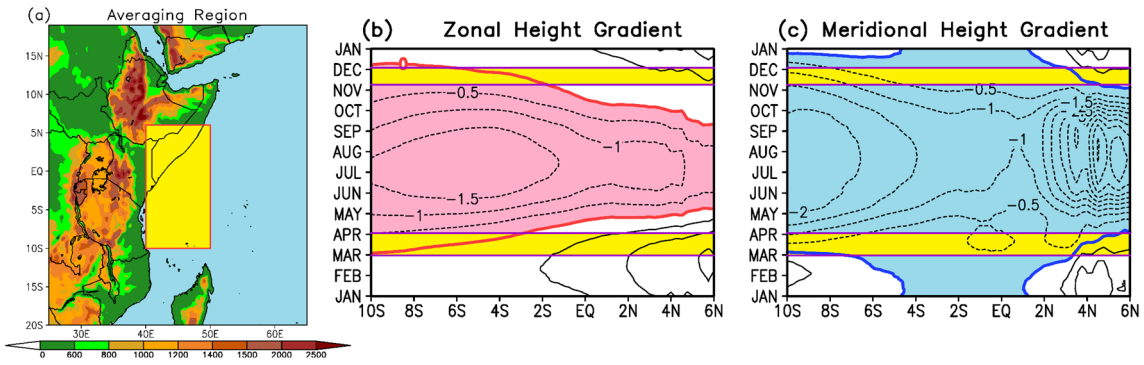

Fig. 3 **a** East Africa topography (m) and location of the analysis region (yellow box) for Fig. 3. ERA5 1979–2018 climatological 30-day smoothed daily 925 hPa **b** zonal and **c** meridional height gradient (meters per 100 km) averaged between 40° E and 50° E. The yellow boxes denote the ERA5 climatological start and end dates of the spring and fall transition periods as listed in Table 1

The climatology shown in Fig. 2 suggest a strong connection between the development of the transition periods and the Mascarene and Arabian Highs. This relationship is examined more closely in Fig. 3, which shows the ERA5 925-hPa climatological annual cycle of the daily zonal and meridional height gradients averaged longitudinally between 40° E–50° E from 10° S to 6° N, the region where the strong low-level cross equatorial flow occurs outside of the spring and fall transition periods (Rodwell and Hoskins 1995; Riddle and Cook 2008). Here, the climatological daily height gradients are examined to better understand how the cross equatorial flow reverses direction during the transition periods. The other reanalyses are similar to ERA5. Figure 3a shows the region for which the height gradients are longitudinally averaged between 10° S and 6° N, while the climatological daily zonal and meridional gradients are shown in Fig. 3b and c, respectively. The yellow strips in Fig. 3b and c indicate the timing of the climatological spring and fall transition periods.

During boreal spring, the start date of the transition period is associated with a reversal of the meridional height gradient from positive to negative south of 6° S (Fig. 3c), accompanied by a shift from westerly to easterly in the zonal component of the flow. This reversal is associated with the breakdown of the SICZ/MCT over the Mozambique Channel (Fig. 2a and b).

The end of the spring transition period is associated with a reversal of the zonal height gradient from positive to negative near 2° S (Fig. 3b) combined with a reversal—from positive to negative—of the meridional gradient at 4° N–6° N. The former is associated with the equatorward seasonal progression of coastal ridging related to the development of the southerly component of the flow off the Tanzanian and Kenyan coast south of the equator. The latter is tied to the ongoing seasonal weakening of the low-level ridging over the Arabian Sea, and is associated with a reversal from easterly to westerly of the low-level zonal flow north of the equator over the Arabian Sea.

A reversal of the meridional height gradient north of 4° N (Fig. 3c) combined with a reversal of the zonal height gradient from negative to positive around 2° S (Fig. 3b) marks the beginning of the fall transition period. The former is associated with the development of an easterly component of the flow north of the equator between 3° N–8° N, while the latter is associated with the development of northerly flow along the coast south of the equator. The end of the transition period is also associated with a reversal of the zonal height gradient from negative to positive, but the reversal extends southward to 10° S in this case. The end of the transition period and the zonal height gradient reversal precede the meridional height gradient reversal associated with the development of the austral summer SICZ/MCT by a couple of weeks, suggesting that the development of the northerly cross equatorial flow influences the development of the SICZ/MCT during the austral winter rather than vice versa.

4.2 Relationship between transition periods and rainfall

With a definition of the spring and fall transition periods, we can quantify the proportion of the total annual rainfall associated with each transition period. Figure 4 shows the spring, fall, and combined spring + fall transition period percentages of the total annual rainfall over East Africa from the ARC2 (Fig. 4a–c) and CHIRPS2 climatologies (Fig. 4d–f). During the spring, ARC2 and CHIRPS2 both indicate that the highest percentages (20–30%) occur over eastern Tanzania. Farther north, the percentages are lower (5–15%) over most of Kenya, Somalia, and southern Ethiopia. An exception is over the Turkana Channel near Lake Turkana where both ARC2 and CHIRPS2 indicate that 15–30% of the total annual rainfall is associated with the spring transition period. The highest percentages, ranging from 20–30% in ARC2 (Fig. 4b) and 20–40% in CHIRPS2 (Fig. 4e), during the fall transition period are located predominantly over the Kenyan coastal plain. Farther south, over the Tanzanian coastal plain, the percentages are much lower, generally less than 10%. When the two transition periods are combined (Fig. 4c and f), the percentages range from 25 to 40% for much of southwestern Somalia, Kenya, and Tanzania with even some higher, more localized percentages ranging from 40 to 55% in areas over eastern Kenya.

While significant percentages of the annual rainfall are delivered during the transitions, the boreal spring long rains and fall short rain periods are longer than the transition periods. However, on interannual time scales, the length of the transition periods are correlated with the seasonal rainfall over large areas of East Africa. Figure 5a–d show correlations between seasonal precipitation estimated from CHIRPS2 and ARC2 and the transition period length from ERA5 for the spring and fall. A widespread positive relationship between the transition period length and boreal spring (March–May) seasonal rainfall extends from central Tanzania northward to southern Ethiopia and Somalia in both datasets. A positive relationship also occurs during the fall (November–December) over Kenya and Uganda (Fig. 5c and d). The results are similar when the ERAI and JRA-55 reanalyses are used, but MERRA2 has only non-significant positive correlations over Kenya and Tanzania during the spring.

Correlations between seasonal rainfall and transition period start and end dates are also examined (Fig. 5e–l). The start date has a significant negative relationship with seasonal rainfall in most of the same areas with significant positive correlations in Fig. 5a–d, indicating that an early start to the transition period presages high seasonal

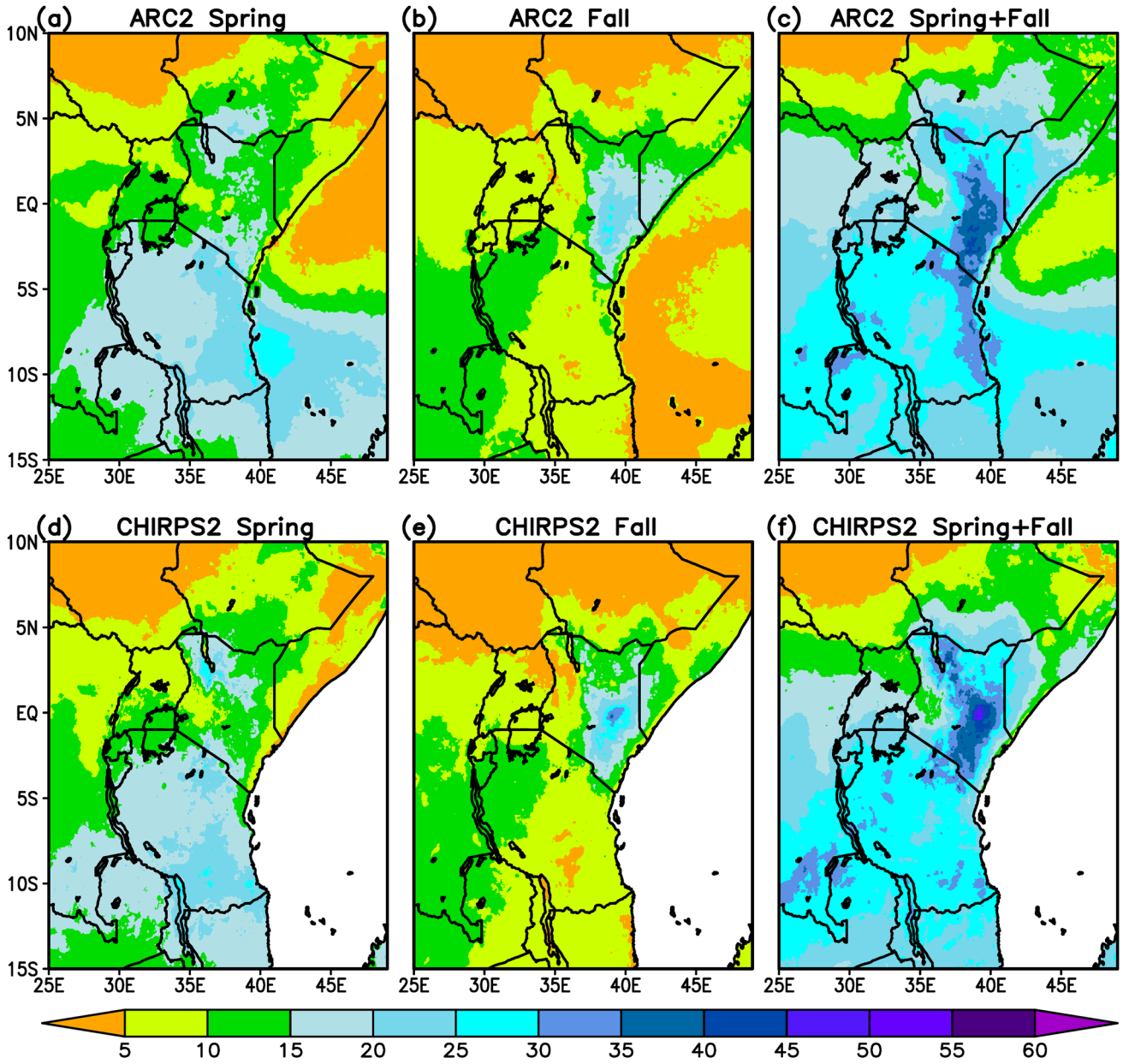

Fig. 4 Percentage of total annual rainfall associated with the **a** spring (March 3–April 3), **b** fall (November 9–December 3), and **c** combined spring + fall transition periods in the ARC2 climatology. **d**–**f** are the same as **a**–**c**, but for the CHIRPS2 climatology

rainfall totals. In fall, the start date of the transition period is negatively correlated with the seasonal rainfall totals, similar to the spring. However, the fall end date (Fig. 5k and l) is also negatively correlation with rainfall totals, indicating that an early (late) end date is associated with higher (lower) seasonal rainfall totals south of 6° S and east of 31° E. This is discussed further in the next section.

4.3 Interannual variability of the boreal spring transition period

Figure 6 shows the time series of the boreal spring transition period length, start date, and end date from the four reanalyses. As shown in Table 2, there is generally a high correlation among the different reanalyses, and all correlations

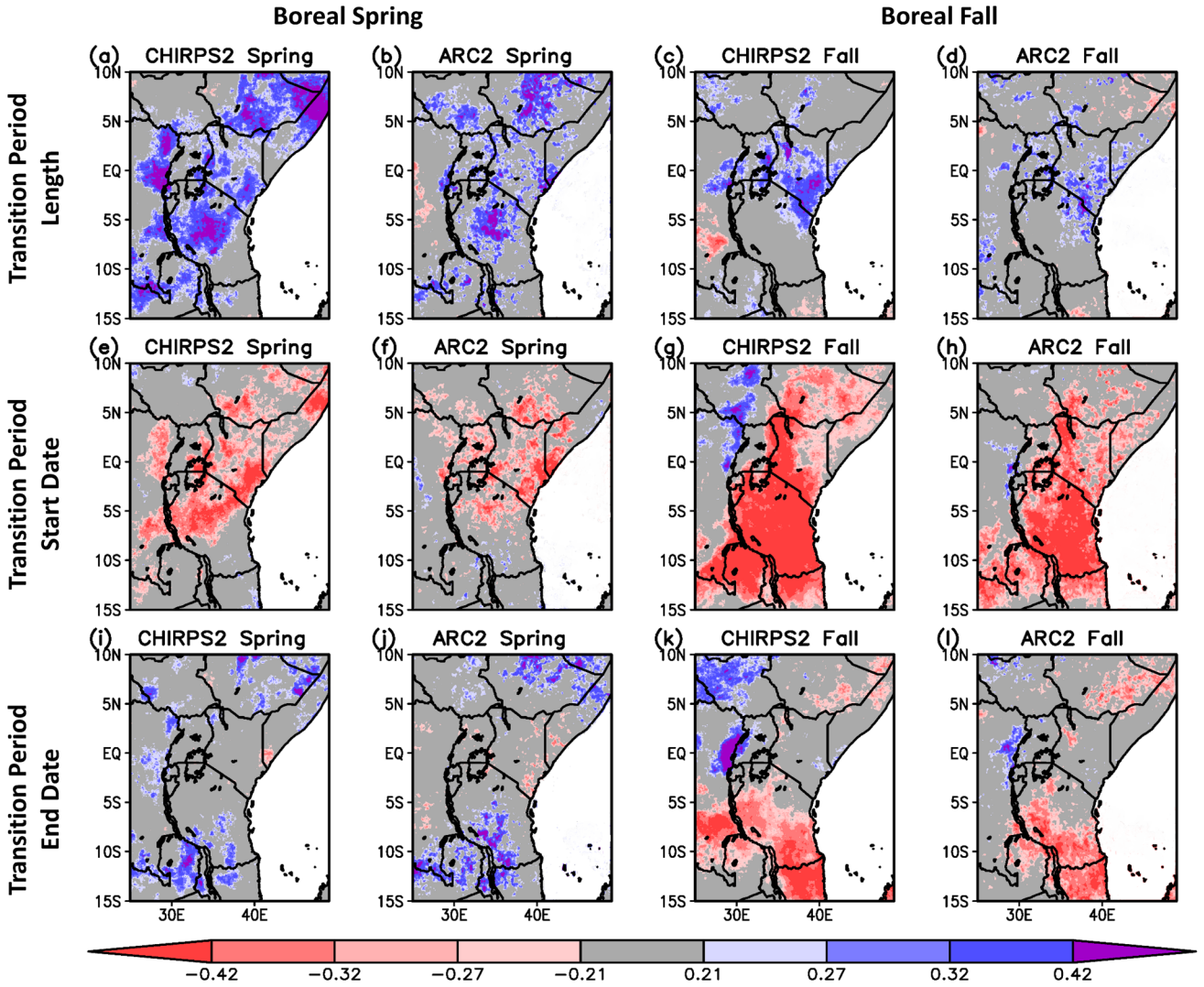

Fig. 5 Correlations between seasonal spring (March–May) and fall (November–December) CHIRPS2 and ARC2 rainfall and **a–d** ERA5 transition period length, **e–h** transition period start date, and **i–l** transition period end date. Only statistically significant correlation values greater than the 80th (±0.21), 90th (±0.27), 95th (±0.32), and 99th (±0.42) percent level of confidence are shaded in color. Gray shading denotes correlation values below the 80th percent level of confidence

are found to be significant at the 99% level of confidence. Spring transition period length correlations range from 0.90 for ERAI-ERA5, to 0.64 for ERA5-MERRA2. Likewise, the start date and end date correlations between the reanalyses are all greater than 0.74 and 0.57, respectively. Thus, while agreement between the reanalyses is good, it is not perfect. For example, all reanalyses suggest a transition period length of around 40 days with a start date around February 20 and end date around April 30 in 1998. In contrast, the agreement among the reanalyses is weaker in 1997 when the transition period length ranges from 20 days in ERA5 to 51 days in JRA-55. While the four reanalyses are in general agreement regarding the start date occurring in early March 1997, the end date ranges from March 20 in ERA5 to April 22 in JRA-55.

Interannual variations in the length of a transition period can be explained by variations in the start date, end date, or both. We define six types of deviations from the climatological means (Table 3) to characterize interannual variations in the transition period length. Three types associated with a short transition period are events when an early end that more than offsets an early start date, referred to hereafter as SEE, events with both a late start and an early end (SLE), and events with a late start that more than offsets a late end (SLL). Long transition periods are those with an early start that more than offsets an early end (LEE), events with both an early start and a late end (LEL), and events with a late end that more than offsets a late start (LLL). For the rare instance when the transition period length, start date, and/or end date equals the climatological mean value for a particular year,

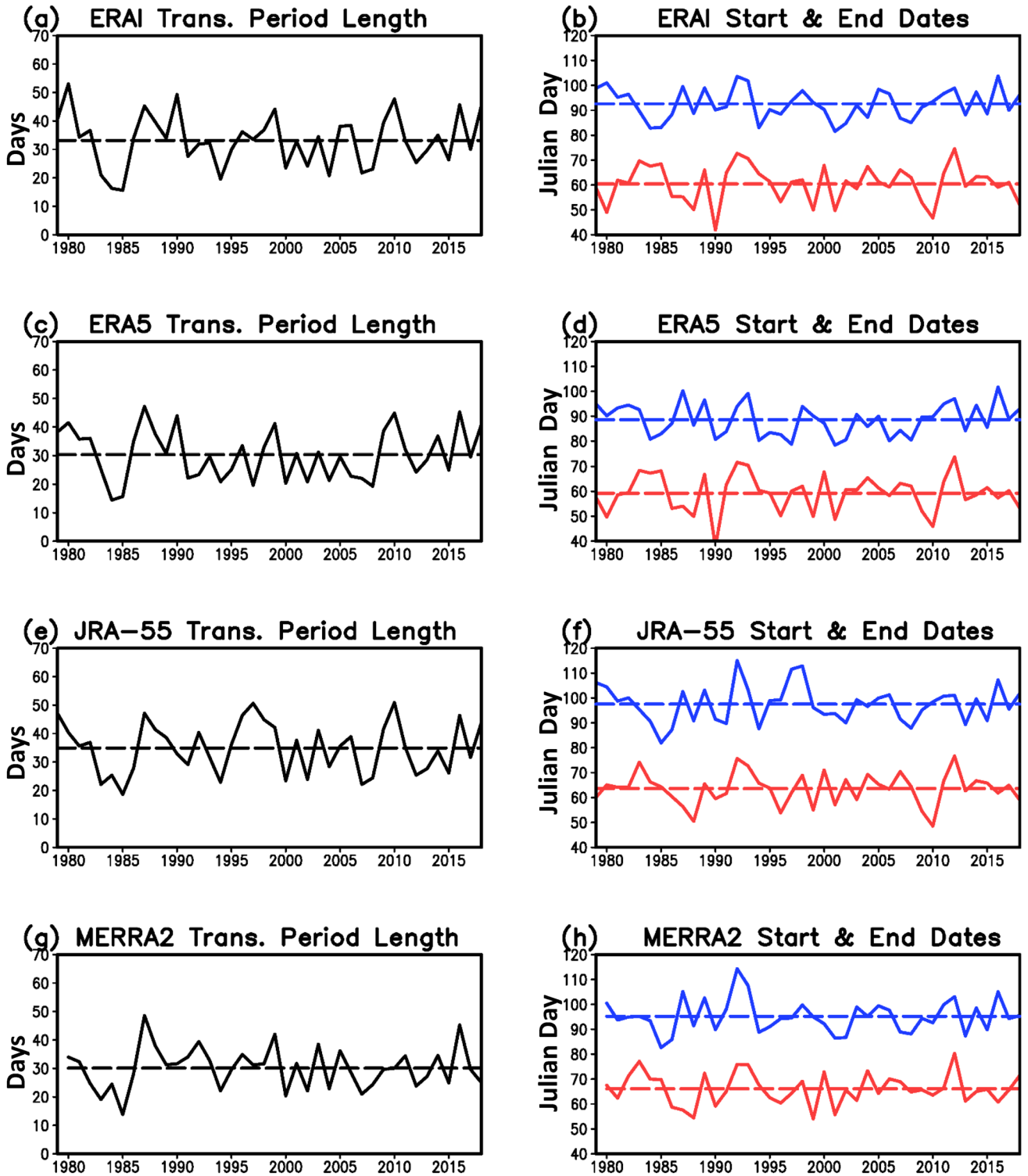

Fig. 6 Boreal spring (left column) transition period length (days) and (right column) transition period start and end date (Julian day) time series for **a**, **b** ERAI, **c**, **d** ERA5, **e**, **f** JRA-55, and **g**, **h** MERRA2. All time series are detrended, with the long-term change removed. Dashed lines denote climatological averages

Table 2 Correlations between the different reanalyses for the boreal spring and fall transition period length, start date, and end date

	ERAI-ERA5	ERAI-JRA55	ERAI-MERRA2	ERA5-JRA-55	ERA5-MERRA2	JRA-55-MERRA2
Spring length	0.90	0.80	0.69	0.67	0.64	0.73
Spring start date	0.98	0.84	0.74	0.82	0.76	0.79
Spring end date	0.81	0.82	0.87	0.57	0.74	0.80
Fall length	0.92	0.90	0.88	0.85	0.82	0.81
Fall start date	0.88	0.75	0.85	0.76	0.85	0.65
Fall end date	0.96	0.94	0.95	0.92	0.88	0.91

Table 3 Listing of common boreal spring and fall transition period event type years among the atmospheric reanalyses

Boreal Spring						Boreal Fall					
SEE	SLE	SLL	LEE	LEL	LLL	SEE	SLE	SLL	LEE	LEL	LLL
2013	1984	2012	1988	1979	1982	1979	1981	1989	1988	1980	1993
	1985		1990	1987	1989	1983	1985		2006	1984	1999
	1994		1996	2010	1998	2007	1987			1992	2000
	2000			2016		2008	1996			2009	2002
	2002			2018		2011	2004			2012	2016
	2004					2017					
	2007										
	2008										
	2015										

it is categorized as "Other" (1 year from ERA5 and 1 year from JRA-55 fall into this category for the spring transition period). Note no condition on the number of days earlier (later) than a climatological date to qualify as early (late) is placed when defining the types. This means a transition period will be classified early or late even if it differs by one day from the climatological date.

Figure 7a shows the boreal spring frequency distributions of the different event types from the four reanalyses, in addition to the multi-reanalysis average. Based on the multi-reanalysis average, 19 of the 40 years are classified as short transition periods, and 21 as long transition periods. Of the 19 short transition periods, the SLE type is more than twice as likely to occur as the SEE or SLL types, suggesting that a late start is correlated with an early end of the spring transition period. The individual reanalyses agree with this result with the exception of MERRA2, which has a higher frequency of SEE events at the expense of the SLE events.

For long transition periods, the LEL pattern occurs most frequently, with a multi-reanalysis average of 8.25 events accounting for approximately 41% of the total number of long transition events, suggesting that long spring transition periods are more likely to be associated with an earlier start and a later end. However, the LEE and LLL transition period types occur more frequently than their short-transition counterparts (SEE and SLL). Again, the distributions from ERAI, ERA5, and JRA-55 generally agree, but MERRA2 suggests that the most events for this type are LEE and not LEL.

Figure 7b–d show scatterplots of the differences from climatology of the transition period length, start date, and end dates from the reanalyses. The gray numbers in each column denote the multi-reanalysis average for each event type. Generally, when the start and end dates work together to change the transition period length (SLE and LEL), the transition period length is at least twice as long as when the start and end date changes are in opposition (SEE, SLL, LEE, LLL). While most of the individual years from the different reanalyses have start and end date differences that fall within ± 10 days of the climatological mean, it is possible to have start and/or end dates differences more than ± 15 days for a given year for a particular reanalysis. However, these outliers tend to be reanalysis dependent, and based on Fig. 7, are not broadly robust across all of the reanalyses.

To form composites of the six transition types, we select years in which the anomalies are similar in multiple reanalyses using the smoothed and detrended data. For an event to be included in a composite, it must agree on the sign of the difference from the climatology for the transition period length (long or short), start date (early or late), and end date (early or late) in at least 3 of the 4 atmospheric reanalyses. Additionally, if one reanalysis does disagree on whether the start and/or end dates are early or late, it still must agree with the other three reanalyses regarding whether the transition period length is long or short in order to be considered. Table 3 shows the boreal spring years for each type that meets these criteria.

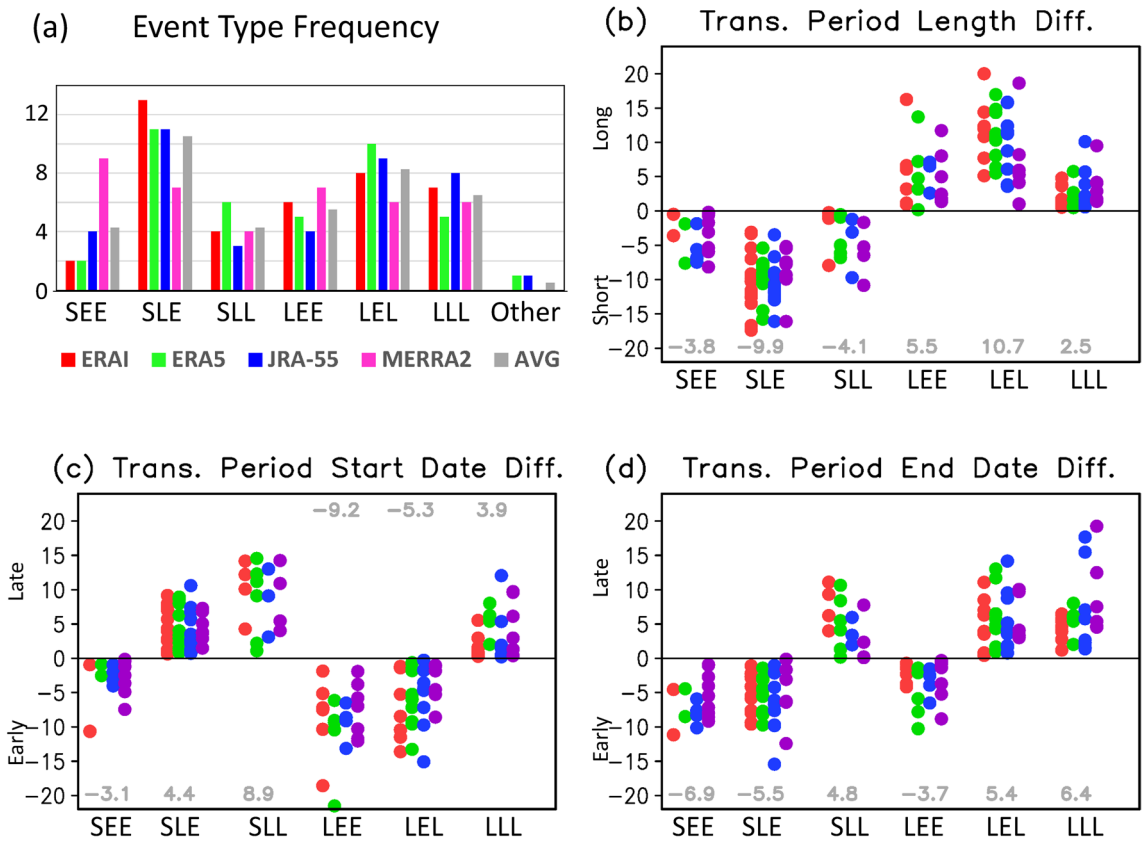

Fig. 7 Boreal spring transition period **a** event type frequency, and transition period **b** length, **c** start date, and **d** end date differences from climatological mean for individual years from the various atmospheric reanalyses (ERAI, ERA5, JRA-55, and MERRA2). Event types include short-early start/early end (SEE), short-late start/early end (SLE), short-late start/late end (SLL), long-early start/early end (LEE), long-early start/late end (LEL), and long-late start/late end (LLL). Other type includes events where the transition period length, start, and/or end dates did not change. Gray denotes the multi-reanalysis average

Two event types, SLE and LEL, yield at least 5 years to form composites and are evaluated. Figure 8 shows 925-hPa geopotential height and wind anomalies for the boreal spring pre-climatological start (10 days before the start date), the transition period, and the post-climatological end (10 days after the end date) for the LEL and SLE types from ERAI. The other three reanalyses are similar to ERAI. Before the start in the LEL case (Fig. 8a), there are significant positive height anomalies over the Mozambique Channel as well as over the central Indian Ocean between 10° S–20° S. The former signifies an early breakdown of the SICZ/MCT, while the latter indicates a northward/northeastward shift of the Mascarene High. Anomalous flow east of 50° E between 5° S and 12° S is easterly, indicating a weakening of the near-equatorial westerlies and a strengthening of the extra-tropical easterlies (Fig. 2a). West of 50° E, the anomalous flow is southerly from 10° S to the equator, indicating a reduction of the cross-equatorial northeasterly flow (Fig. 2a). North of the equator, height and wind anomalies are generally weak and not found to be significant at the 80% level of confidence, suggesting the early start is largely associated with circulation changes over the South Indian Ocean.

The only significant height anomalies during the LEL transition period (Fig. 8b) and after its end (Fig. 8c) are located south of Madagascar, with negative height anomalies indicating a weakening of the westward extension/development of the Mascarene High (Fig. 2b, c). Significant anomalous northerly flow occurs along the Kenyan and Tanzanian coast in association with a delayed development of the austral winter low-level ridging over this region (Fig. 2c). Positive height anomalies north of the equator over the Indian Ocean, while not significant, are associated with anomalous easterly flow along and just north of the equator, indicating a weakening of the equatorial westerly flow over this region.

Figure 8d–f show the 925-hPa height and wind anomalies for the SLE composite. The anomalies for the pre-climatological start (Fig. 8d), the transition period (Fig. 8e), and the post-climatological end (Fig. 8f) are largely opposite to those of the LEL case (Fig. 8a–c). The most notable difference is that the anomalous low-level flow along the East African coast and to the east of Madagascar is more spatially

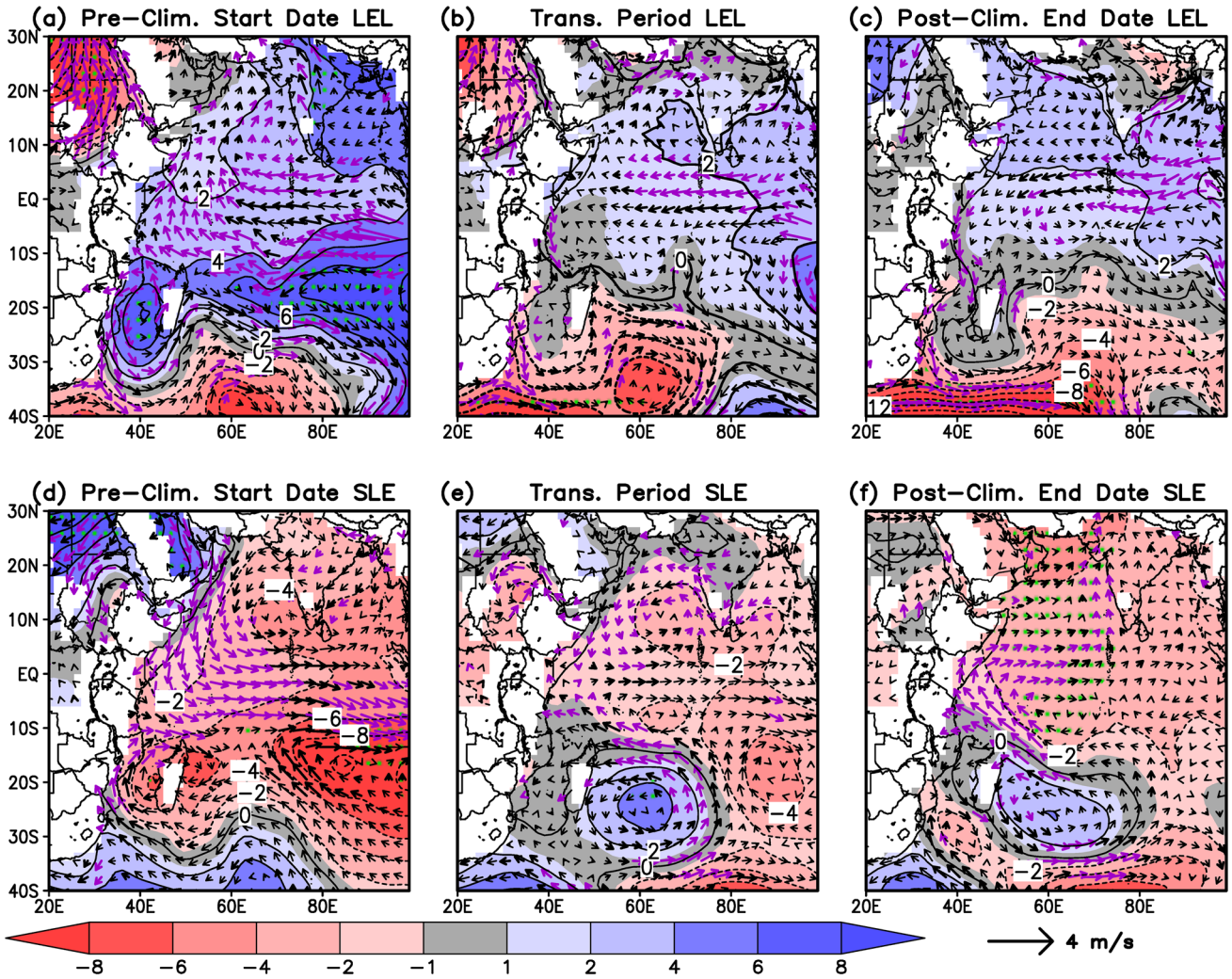

Fig. 8 ERAI long-early start/late end (LEL) 925 hPa geopotential height (shading; m) and wind (vectors; m s^{-1}) composite anomalies for **a** the 10-days prior to the defined climatological ERAI spring transition period start listed in Table 1, **b** the spring transition period, and **c** the 10-days after the defined climatological ERAI spring transition period end listed in Table 1. **d**–**f** are similar, except they are for the short-late start/early end (SLE) composite. Green stippling denotes height anomalies significant at the 90% level of confidence, while black (purple) bolded vectors denote winds significant at the 80% (90%) level of confidence

robust for the transition period and post-climatological end in SLE compared to LEL. This may be partially due to the composite sample size being larger for SLE (9 events) than LEL (5 events).

Figure 9a and b show climatological spring transition period average rainfall rates from CHIRPS2 and ARC2, respectively, while Fig. 9c, d show the climatological March–May average rainfall. The largest boreal spring transition period rainfall rates occur south of the equator over Tanzania and over the Rift Valley highlands along 30° E in the climatology (Fig. 9a, b), while they are shifted more northward over the equatorial Highland/Lake Victoria region in the seasonal average (Fig. 9c, d). Figure 9e–l show the precipitation anomalies for the LEL and SLE events for the transition period and March–May seasonal average.

For the spring transition period, the largest and most significant rainfall anomalies in both the LEL and SLE composites occur north of 4° S where climatological transition period rainfall rates are lower. For the LEL case, both CHIRPS2 and ARC2 produce widespread positive rainfall anomalies over much of East Africa between 12° S–10° N, with the most robust changes over the southeastern Ethiopian Highlands, western South Sudan, and in the vicinity of Lake Victoria (Fig. 9e, f). Both CHIRPS2 and ARC2 indicate more localized reductions in rainfall along coastal Tanzania and southeastern Congo, but these differences are not significant at the 90% level of confidence. For the SLE case (Fig. 9i, j), CHIRPS2 and ARC2 agree on a widespread reduction in rainfall over East Africa, with significant anomalies at the 90% level of confidence

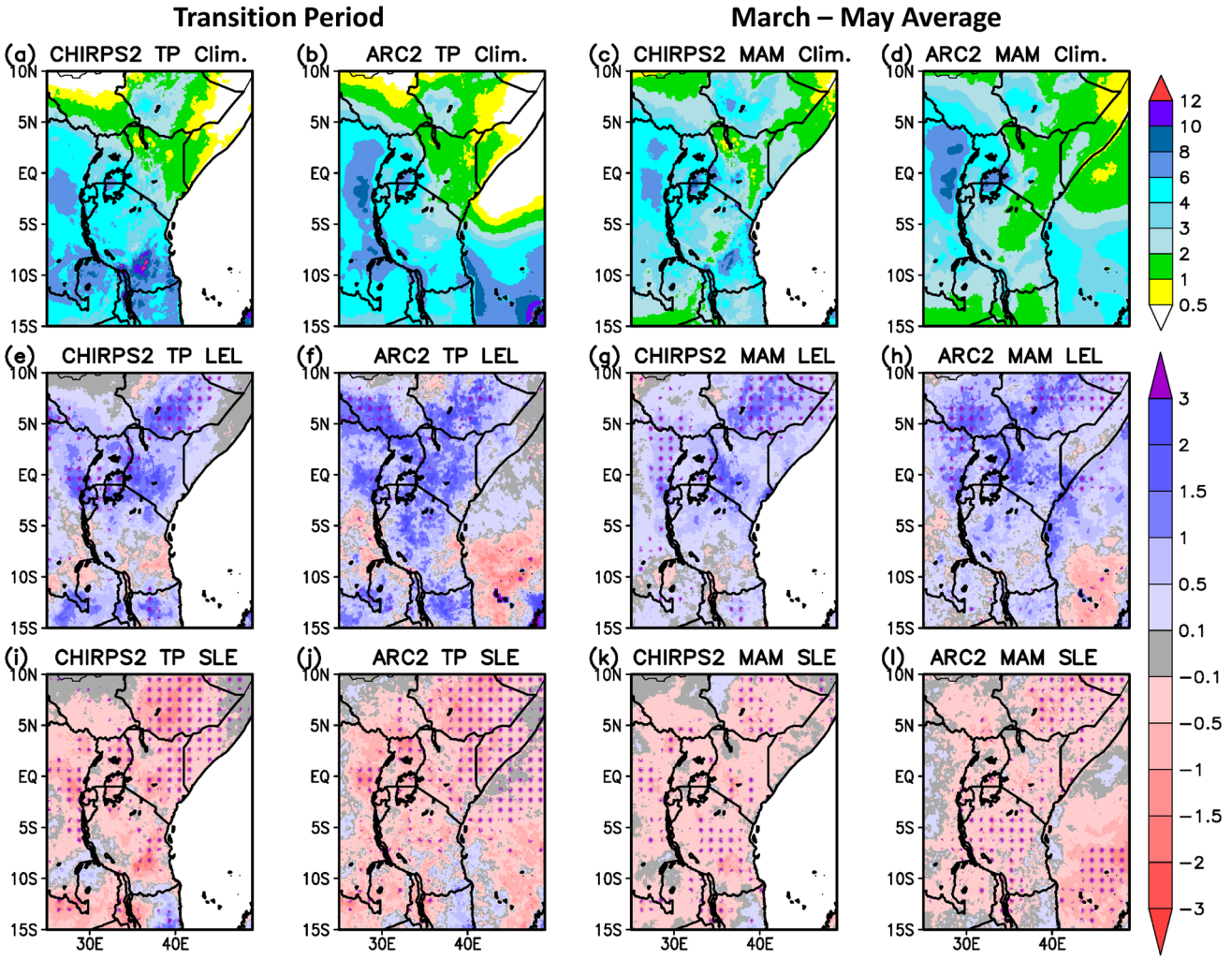

Fig. 9 Spring transition period climatological precipitation rate (mm day^{-1}) for **a** CHIRPS2, and **b** ARC2, and March–May climatological precipitation rate for **c** CHIRPS2, and **d** ARC2. Also **e** CHIRPS2 and **f** ARC2 spring long-early start/late end (LEL) composite average transition period precipitation anomalies, and **g** CHIRPS2 and **h** ARC2 March–May precipitation anomalies. **i**–**k** are similar to **e**–**h** except they are for the short-late start/early end (SLE) composite type. Purple stippling denotes rainfall anomalies significant at the 90% level of confidence

generally north of 5° S over the Lake Victoria region, the southern Ethiopian Highlands, and the coastal plains of Kenya and Somalia. Agreement between CHIRPS2 and ARC2 is not as strong over southeastern Tanzania, where CHIRPS2 indicates significant negative anomalies but ARC2 has weak positive anomalies.

A comparison of the spring transition period rainfall anomalies to the March—May seasonal precipitation anomalies indicates that for LEL (Fig. 9e–h) and SLE (Fig. 9i–l) event types the transition period anomalies are generally similar to the seasonal rainfall anomalies. This suggests that while the spring transition period is only part of the East African long rains season, the transition period precipitation anomalies are reflective of the seasonal rainfall variability over East Africa for LEL and SLE event types.

Figure 10a and b show surface temperature anomalies for ERAI and JRA-55 in the LEL spring transition period composite, while Fig. 10c, d show surface temperature anomalies for the SLE composite. JRA-55 is shown along with ERAI because, unlike the other reanalyses, its prescribed SSTs are from Centennial In Situ Observation-based Estimates (Ishii et al. 2005) which are based on in situ measurements and do not include satellite-derived SST estimates. Despite the difference in SSTs, the areas of significant SSTAs are consistent between ERAI and JRA-55 over the Indian Ocean. LEL is associated with significantly warmer SSTs along the Somali coast, in the Mozambique Channel, and over the southwestern Indian Ocean between 50° E and 70° E from 10° S to 25° S, with anomaly magnitudes consistent between ERAI and JRA-55 (Fig. 9a, b). For the SLE case (Fig. 10c,

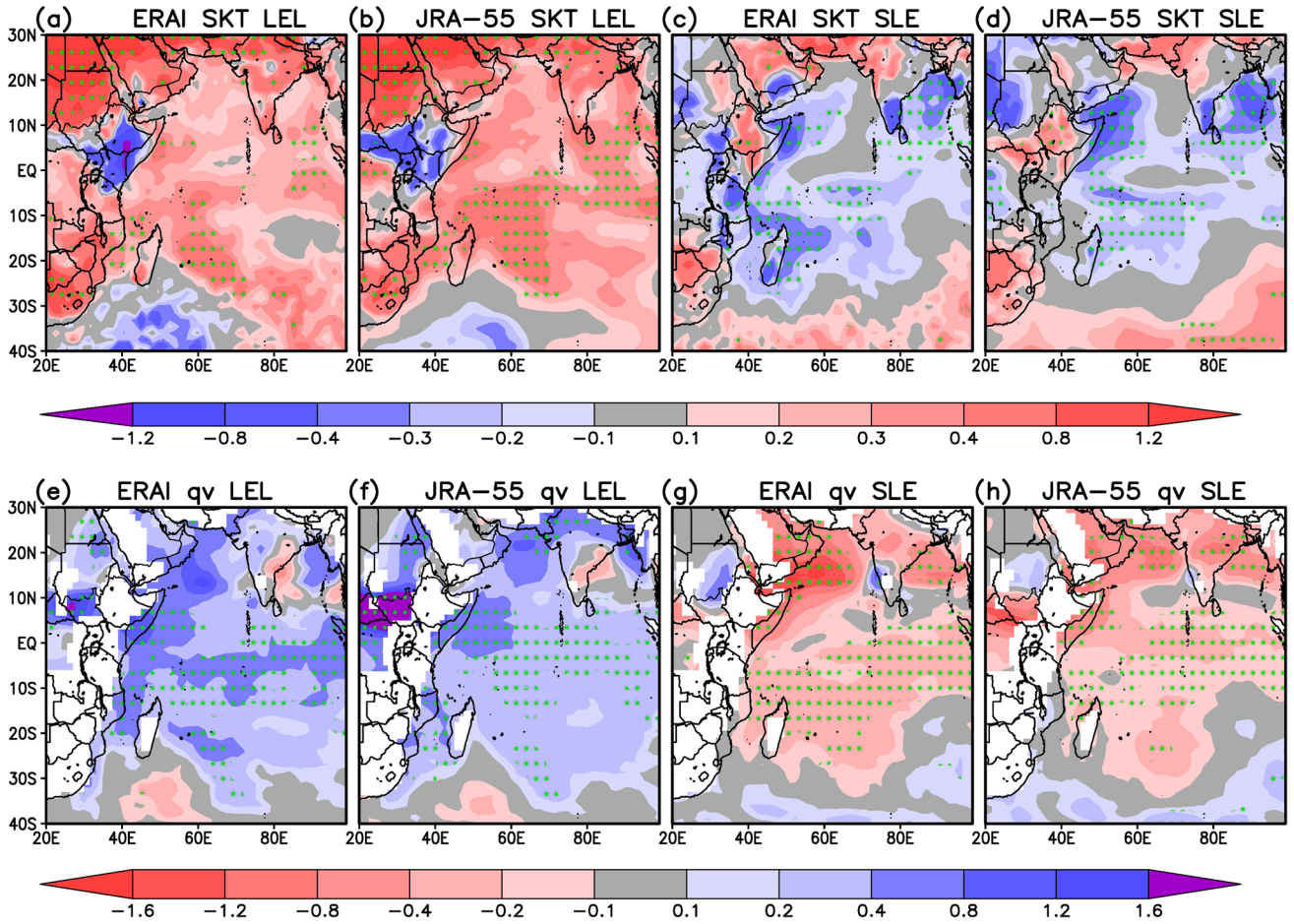

Fig. 10 Spring transition period LEL composite surface skin temperature anomalies (K) for **a** ERAI, and **b** JRA-55. **c** and **d** are similar to (**a**) and (**b**) except they are for the SLE composite type. Spring transition period LEL composite 925 hPa specific humidity (g kg^{-1}) for **e** ERAI, and **f** JRA-55. **c** and **d** are similar to (**a**) and (**b**) except they are for the SLE composite type. Stippling denotes anomalies significant at the 90% level of confidence

d), SSTAs are significantly cooler along the Somali coast and over the southwestern Indian Ocean between 50° E and 70° E from 10° S to 25° S, but anomaly magnitudes differ in the two reanalyses. Additionally, ERAI produces significant cooling between 10° S and 20° S off the Tanzania/Mozambique coast, where JRA-55 indicates minimal cooling.

The composites indicate that there is a relationship between SSTAs in the western Indian Ocean and the anomalous low-level circulation during the spring transition period. Cold SSTAs during SLE events are associated with the anomalous ridging to the east of Madagascar and stronger cross-equatorial flow along the Kenya/Somalia coast (Fig. 8e, f). The former is likely associated with the equatorward and westward transport of cooler SSTs from the mid-latitudes south of the equator, while the latter is likely associated with enhanced coastal upwelling of cooler SSTs north of the equator off the coast of Somalia. The opposite occurs for the LEL case, although the wind anomalies are generally weaker for the LEL case than for the SLE case. This region is known to exhibit strong air-sea coupling (McClanahan 1988; Swallow et al. 1991; Varela et al. 2015; Nigam et al. 2018).

Figure 10e and f show the 925-hPa spring transition period specific humidity anomalies from ERAI and JRA-55 from the LEL composites, while Fig. 10g, h show specific humidity anomalies for the SLE composite. Warmer SSTAs in the LEL case are associated with an increase in the low-level moisture content over the Indian Ocean basin, with the largest increases over the warmest SSTAs along the Somali/Kenyan coast. This increase in the atmospheric moisture content, and not an enhancement of the low-level easterly flow, is responsible for the enhanced rainfall rates during spring LEL events (Fig. 8b). The opposite is true for the SLE case, as the decrease in atmospheric moisture associated with cooler SSTAs, and not a weakening of the onshore low-level easterly flow (Fig. 8e), is associated with the reduced rainfall rates over East Africa (Fig. 9e, f).

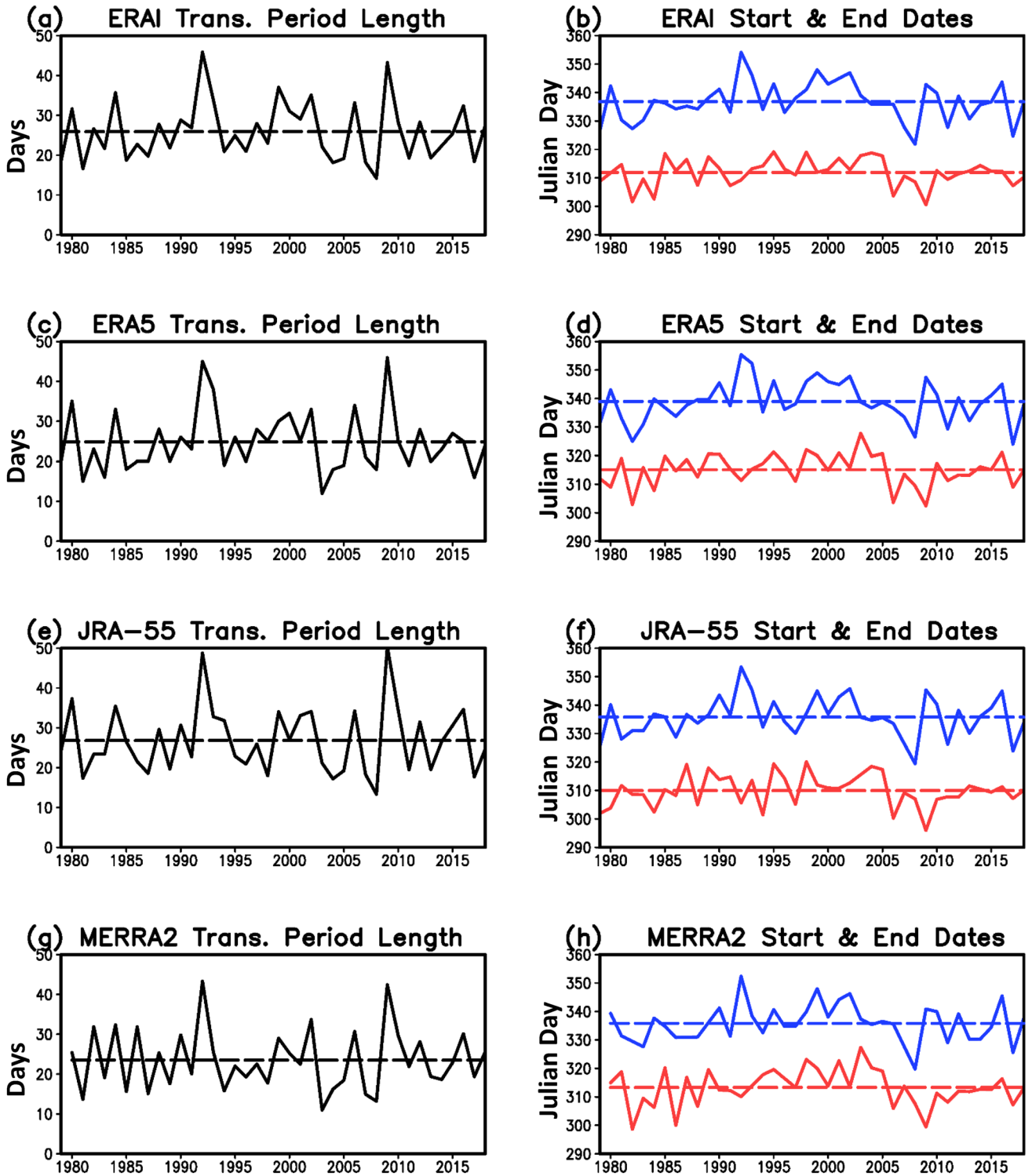

Fig. 11 Boreal fall (left column) transition period length (days) and (right column) transition period start and end date (Julian day) time series for **a**, **b** ERAI, **c**, **d** ERA5, **e**, **f** JRA-55, and **g**, **h** MERRA2. All time series are detrended, with the long-term change removed. Dashed lines denote climatological averages

4.4 Interannual variability of the boreal fall transition period

Interannual variations in the boreal fall transition season length, start date, and end date from the four reanalyses are shown in Fig. 11. Variations in transition period length and start date are smaller than for the spring transition, as confirmed by the standard deviations in Table 1. In most cases, the transition period length variations fall within ± 10 days of the climatological mean, but there are some years that have transition periods close to 50 days in length, and others that have period lengths around 15 days. Figure 11 and Table 2 indicates agreement among the reanalyses with correlations between reanalyses ranging from 0.92 (ERA5–ERAI) to 0.81 (JRA-55–MERRA2) for the transition period length, 0.88 (ERA5–ERAI) to 0.65 (JRA-55–MERRA2) for the start date, and 0.96 (ERA5–ERAI) to 0.88 (ERA5–MERRA2) for the end date. All correlations are found to be significant at the 99% level of confidence.

Figure 12a shows the frequency of the boreal fall event types in the four reanalyses and the multi-reanalysis average. The short transition period types, SLE and SEE, are most common, with 8.75 years and 8.25 years, respectively, in the multi-reanalysis average. The ERAI and ERA5 reanalyses produce SLE events most frequently, while the JRA-55 and MERRA2 reanalyses produce SEE events most frequently. For the long transition, the LEL (6.75 years) and LLL (7.5 years) types are most common; the four reanalyses are in good agreement regarding the number of events for LEL, but less so for LLL. In general, the consensus among the reanalyses is not as strong as for boreal spring (Fig. 7a).

Figure 12b–d show scatterplots of the differences from climatology of the transition period length, start date, and end dates from the reanalyses. For the most part, the spread

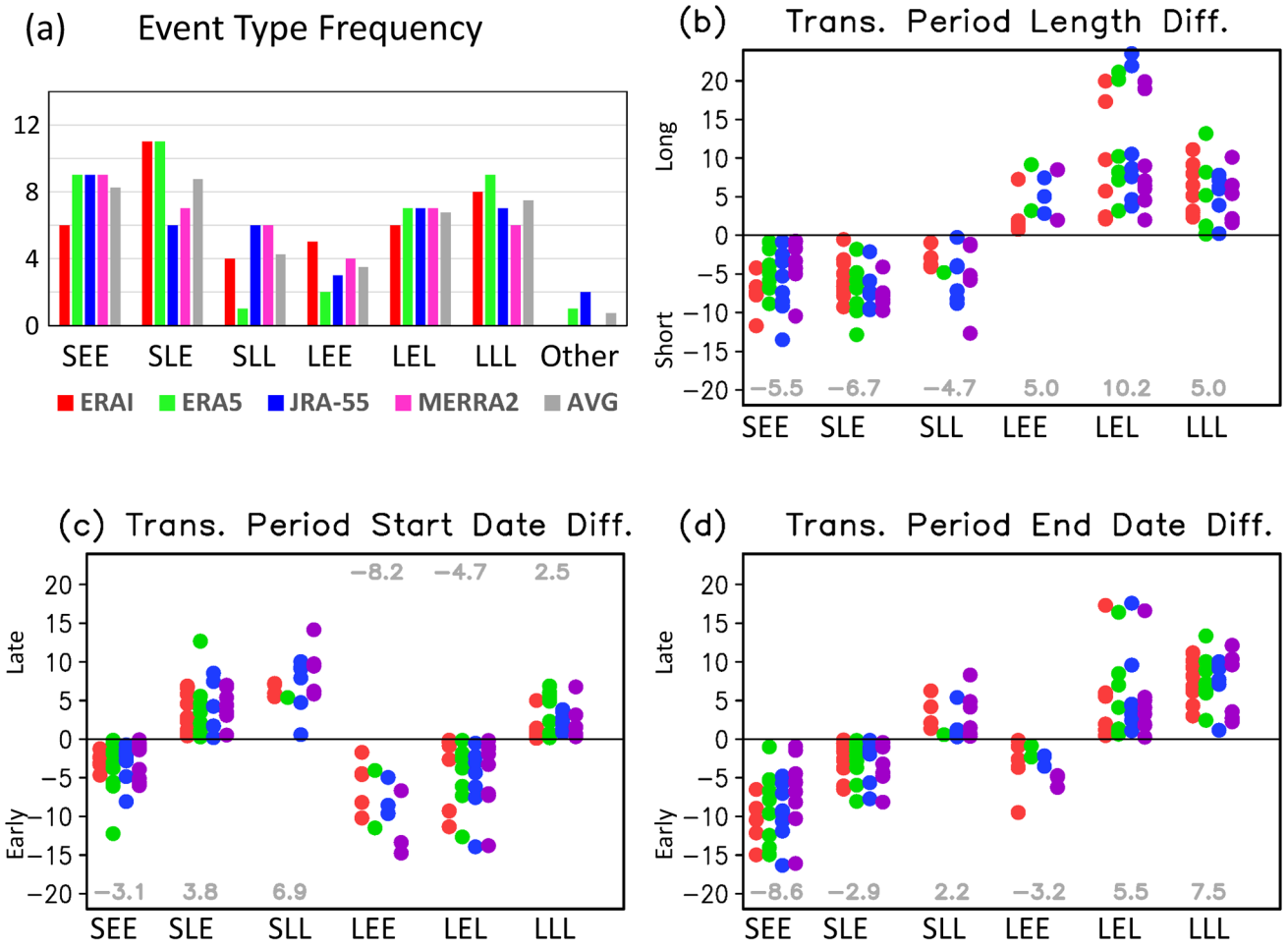

Fig. 12 Boreal fall transition period **a** event type frequency, and transition period **b** length, **c** start date, and **d** end date differences from climatological mean for individual years from the various atmospheric reanalyses (ERAI, ERA5, JRA-55, and MERRA2). Event types include short-early start/early end (SEE), short-late start/early end (SLE), short-late start/late end (SLL), long-early start/early end (LEE), long-early start/late end (LEL), and long-late start/late end (LLL). Other type includes events where the transition period length, start, and/or end dates did not change. Gray denotes the multi-reanalysis average

of the individual event lengths, start dates, and end dates, appears consistent among the various reanalyses. For the SEE, SLE, and SLL types, the transition period length is typically within 10 days of the climatological average aside from a few outliers that are not robust across the reanalyses (Fig. 12b). While SEE type events are dominated by the early end date (Fig. 12d), the SLE events have approximately an equal weighting between differences in the start date (3.8 days late) and end date (2.9 days early). LEE, LEL, and LLL transition period lengths generally fall within 10 days of the mean, but for the LEL type there is a secondary cluster near 19 days that is robust over all reanalyses. As inferred from Fig. 11, this cluster of outliers consists of two years, 1992 (an ENSO neutral year) and 2009 (an ENSO warm year). While remote forcing such as ENSO may be influential in some years, a coherent pattern representing influence from ENSO does not emerge from the analysis.

As shown in Table 3, four event types (SEE, SLE, LEL, and LLL) occur in at least 5 years, and these are used for compositing. Figure 13a–d show the pre-climatological start 925-hPa geopotential height and wind anomaly composites for the LEL, LLL, SLE, and SEE event types, respectively. For the LEL case (Fig. 13a), geopotential heights are anomalously low over the western Indian Ocean west of 65° E and south of 6° N, and anomalously high over the Arabian Sea and the central South Indian Ocean. This suggests an early retreat of the Mascarene High. Over the Arabian Sea, low-level ridging is enhanced in association with a stronger meridional low-level height gradient between 3° N and 10° N. Combined, these circulation anomalies are associated with significantly enhanced easterly flow from India to Somalia, and weaker low-level southeasterly flow from the equator to 10° S along the coast.

The SEE composite (Fig. 13d) also places negative height anomalies over the southwestern Indian Ocean. However, in contrast to the LEL case, the negative height anomalies extend across the Indian Ocean basin north of 40° S. The low-level flow anomaly is weaker than in the LEL case, particularly north of the equator. The most notable significant wind anomalies occur from the Kenya/Tanzania coast to east of Madagascar. The anomalous northwesterly flow is

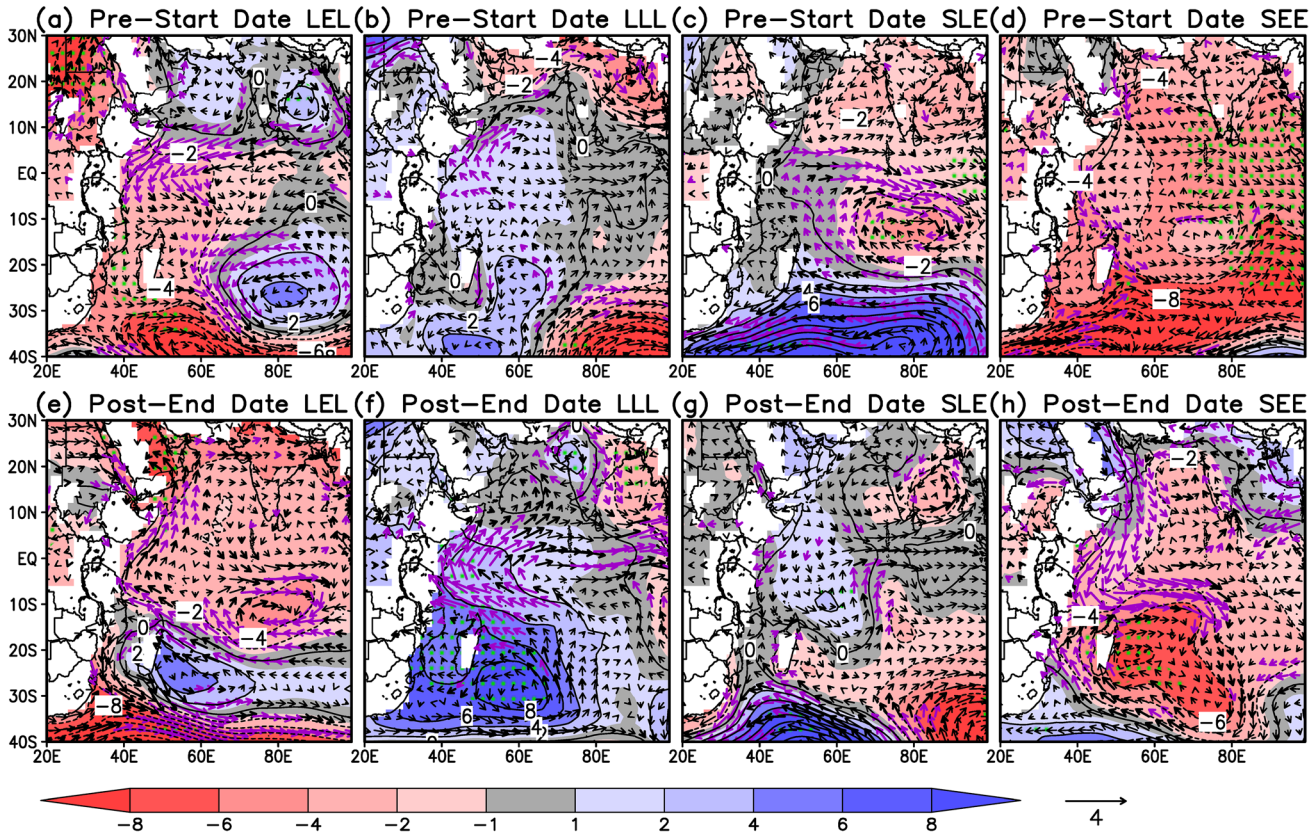

Fig. 13 ERAI **a** LEL, **b** LLL, **c** SLE, and **d** SEE 925 hPa geopotential height (shading; m) and wind (vectors; m s^{-1}) composite anomalies for the 10-days prior to the defined climatological ERAI fall transition period start date listed in Table 1. **d**, **f** Are similar, except they are for the composite anomalies 10-days after to the defined climatological ERAI fall transition period end date listed in Table 1. Green stippling denotes height anomalies significant at the 90% level of confidence, while black (purple) bolded vectors denote winds significant at the 80% (90%) level of confidence

associated with a weakening of the wintertime ridging and the low-level southeasterly flow.

The two composites associated with a late start in boreal fall, LLL (Fig. 13b) and SLE (Fig. 13c), are dissimilar. LLL cases are associated with anomalously high heights over the equatorial and southwestern Indian Ocean, and anomalous southwesterly flow along the Somali coast indicating a weakening of the low-level northeasterly flow that is typical during this time (Fig. 2d). In contrast, there is a significant response in the low-level heights over the South Indian Ocean in the SLE case (Fig. 13c), with anomalously low heights centered around 10° S and 80° E and anomalously high heights south of 25° S indicating a stronger Mascarene High. North of the equator heights are also anomalously low over the Arabian Sea, indicating weaker low-level ridging associated with anomalous westerly flow.

Figure 13e–h show the LEL, LLL, SLE, and SEE geopotential height and wind anomalies after the climatological end at 925 hPa. The most robust and significant height anomalies occur for LLL (Fig. 13f) and SEE (Fig. 13h) events. The LLL composite has positive height anomalies over the Mozambique Channel that extend eastward over the southwestern Indian Ocean, indicating a weaker/delayed development of the SICZ/MCT. The low-level southeasterly flow between the equator and 20° S remains stronger than normal as the northeasterly cross-equatorial flow is slower to develop. The SEE composite (Fig. 13h) is opposite to the LLL anomalies, with negative height anomalies over the southwestern Indian Ocean indicating a stronger/earlier development of the SICZ/MCT accompanied by weaker southeasterly flow between the equator and 10° S and enhanced northeasterly cross-equatorial flow. A noticeable distinction between these two cases is that the anomalous low-level flow extends from the Arabian Peninsula to Mozambique in SEE events, but not LLL events. The SEE low-level flow pattern is indicative of cold air surges along the African Highlands that have been observed to be influential over East Africa (Metz et al. 2013; Vizy and Cook 2014; Crossett and Metz 2017).

The anomalies in the LEL (Fig. 13e) and SLE (Fig. 13g) composites are generally weaker and less significant than those for LLL and SEE. For the LEL case there is evidence of positive height anomalies extending from Mozambique southeastward past Madagascar, but the weak negative height anomalies over the Indian Ocean basin north of 17° S and significant southwesterly wind anomalies along the coast from Mozambique to the Arabian Peninsula suggest the opposite of a cold air surge-like response. For the SLE case (Fig. 13g), the anomalies are localized and weak, and no confident interpretations can be drawn.

Overall, Fig. 13e–h indicate a strong relationship between the transition period end date and the development of the SICZ/MCT. An early end date is associated with an earlier than normal development of the SICZ/MCT that leads to increased seasonal rainfall over southern Tanzania and Mozambique. The opposite occurs for a later than normal end date. As discussed above the robustness of this response depends upon the event type, as the response is stronger for LLL and SEE, but still apparent for LEL and SLE. Physically, this explains the robust negative correlations between the boreal fall end date and the seasonal rainfall in Fig. 5k, l over southern Tanzania and Mozambique.

Surface temperature composite anomalies from ERAI from the pre-climatological start and post-climatological end for boreal fall are shown in Fig. 14a–d and Fig. 14e–h, respectively. Unlike the spring transition period (Fig. 10a–d), the LEL and SLE cases are not accompanied by widespread and significant SSTA anomalies along the coast. The LLL case (Fig. 14b and f) is associated with significantly cooler SSTAs south of the equator from the Kenya coast to east of Madagascar that are consistent with stronger ridging and anomalous low-level southeasterly flow (Fig. 14f). In the SEE composite (Fig. 14d and h) a dipole-like pattern with cooler SSTAs over the western equatorial Indian Ocean and western Arabian Sea, and warmer SSTAs in the Mozambique Channel extending to the east of Madagascar, occurs.

Figure 15a–j show CHIRPS2 and ARC2 fall transition period climatological precipitation rates and composite fall transition period rainfall anomalies. The CHIRPS2 and ARC2 datasets are in agreement. Near the rainfall maximum over coastal Kenya (Fig. 15a and f), there is an increase in fall transition period rainfall rates in LEL and LLL, and a decrease in SLE and SEE. Except for the SLE event type, these differences are not found to be significant at the 90% level of confidence.

There are more robust rainfall anomalies elsewhere. The LEL, LLL, and SLE composites have similar rainfall anomaly patterns, with lower than average rainfall rates north of the equator over southern Ethiopia and Somalia. This is where rainfall rates are typically less intense in the climatology (Fig. 15a and f). For LEL, while the low-level northeasterly flow over Somalia and along the coast may start out being stronger than normal at the beginning of the transition period (Fig. 13a), the flow eventually weakens resulting in reduced low-level wind convergence (not shown) and convection over this region. In contrast, the low-level northeasterlies near the Somali coast remain weak throughout the entire transition period for the LLL case, and the low-level wind convergence (not shown) and rainfall rates also remain weak over southern Ethiopia and Somalia. For the SLE case, the lower rainfall rates are associated with weaker than normal onshore easterly flow at the beginning of the transition period (Fig. 13c).

Rainfall rates are enhanced south of 5° S over southern Tanzania for the LEL and LLL cases, and this enhancement is associated with an intensification of the low-level

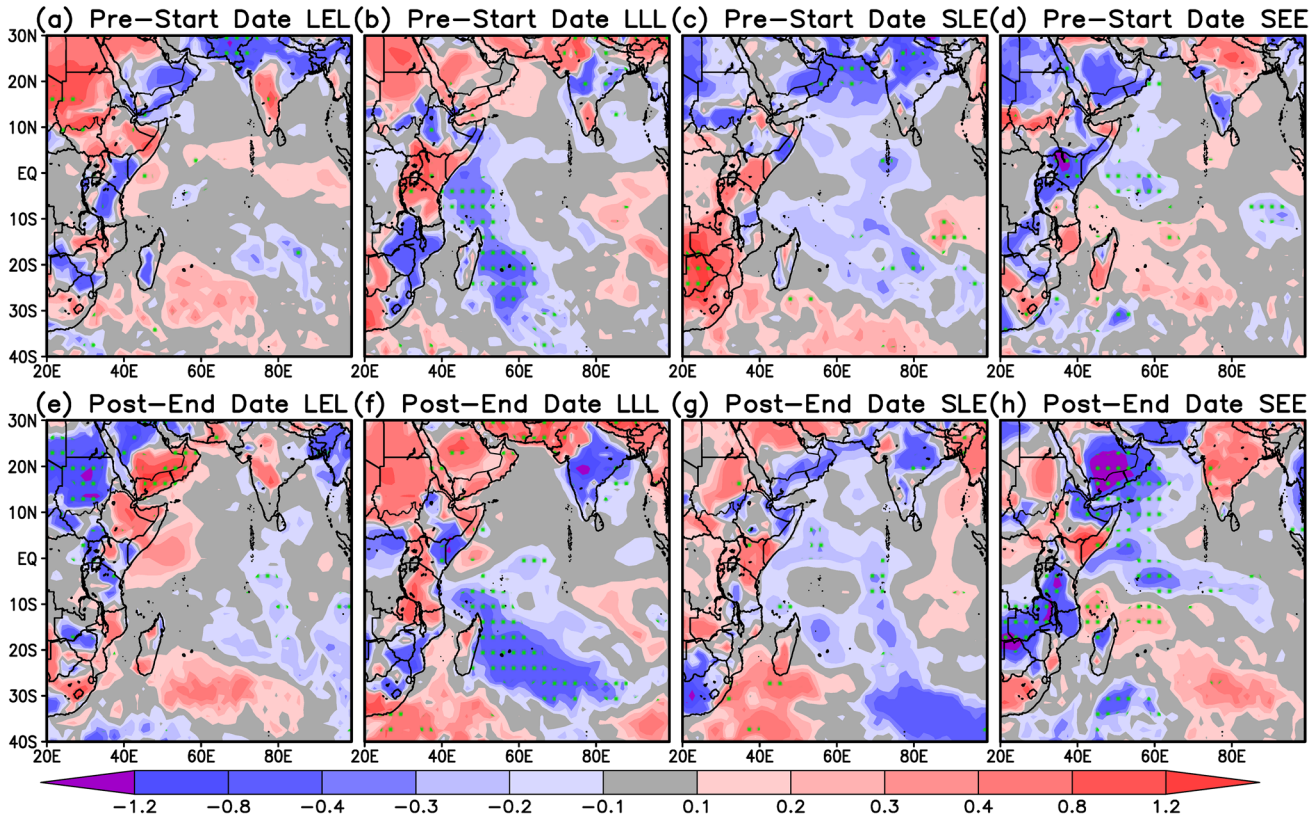

Fig. 14 ERAI **a** LEL, **b** LLL, **c** SLE, and **d** SEE surface skin temperature (shading; K) composite anomalies for the 10-days prior to the defined climatological ERAI fall transition period start listed in Table 1. **d**, **f** Are similar, except they are for the composite anomalies 10-days after to the defined climatological ERAI fall transition period end listed in Table 1. Green stippling denotes values significant at the 90% level of confidence

southeasterly flow from the southwestern Indian Ocean later during the transition period (Fig. 13b and d). The SLE case is also associated with enhanced rainfall over southern Tanzania, with anomalously warm SSTAs in the Mozambique Channel south of 20° S that are associated with an increase in the low-level moisture content over Mozambique and southern Tanzania later during the transition period (not shown).

Rainfall rate composites for the SEE case (Fig. 15e and j) have enhanced rainfall rates north of the equator over southern Ethiopia and Somalia, and reduced rainfall rates south of the equator over southern Tanzania. The former is associated with a strengthening of the coastal low-level northeasterly flow during the transition period (Fig. 13h) that enhances the low-level wind convergence and rainfall intensity over Ethiopia and Somalia. The latter is associated with earlier than normal weakening of the low-level southeasterly flow from the southwestern Indian Ocean between 5° S and 13° S (Fig. 13d) that weakens the low-level wind convergence and rainfall.

Figure 15k–t show the CHIRPS2 and ARC2 November—December seasonal climatological precipitation rates and composite rainfall anomalies. Compared to the fall transition period climatology (Fig. 15a and f), the November—December climatological rainfall rates are generally larger south of the equator, and lower north of the equator (Fig. 15k and p). LEL (Fig. 15l and q) and SLE (Fig. 15n and s) seasonal composite rainfall anomalies are similar to the corresponding transition period anomalies, suggesting that the transition period rainfall variability is largely reflective of the seasonal rainfall variability over East Africa for these two event types. For LLL (Fig. 15m and r), there is only partial agreement between the transition period rainfall anomalies and seasonal precipitation anomalies. This agreement occurs primarily north of 4° N over southern Ethiopia and central Somalia where significant anomalies at the 90% level of confidence are located for this type of event. South of the equator, anomaly patterns are generally opposite of one another, but neither for the transition period or the seasonal average, are the anomalies found to be significant. For SEE (Fig. 15o and t), other than over the Kenyan coastal plains and the highlands west of Lake Victoria, the composite rainfall anomaly patterns for the transition period and November—December

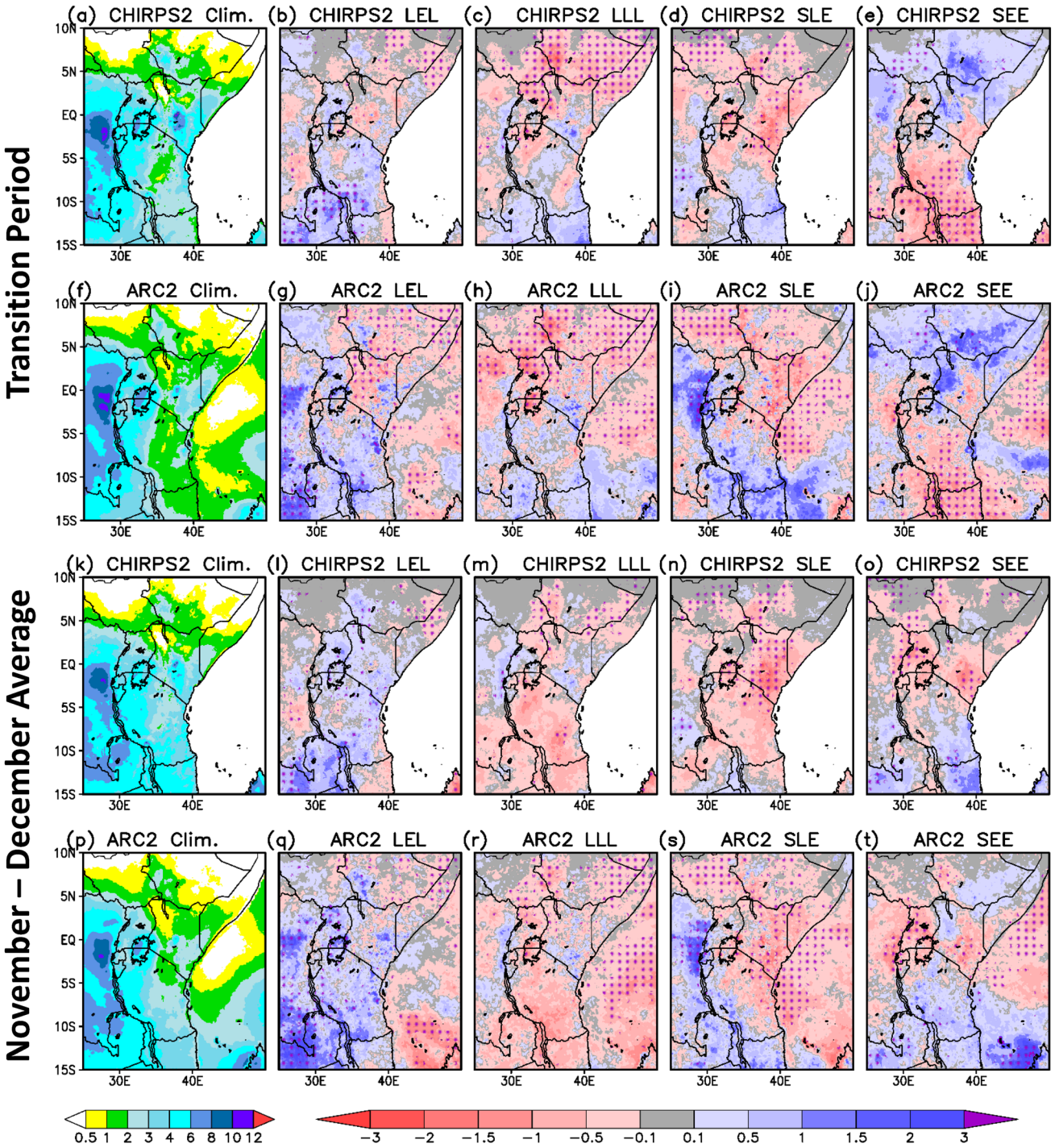

Fig. 15 Fall transition period **a** climatological precipitation rate (mm day^{-1}), and **b** long-early start/late end (LEL), **c** long-late start/late end (LLL), **d** short-late start/early end (SLE), and **e** short-early start/early end (SEE) composite average precipitation anomalies (mm day^{-1}) for CHIRPS2. **f**–**j** Are the same as (**a**–**e**), respectively, except they are for ARC2. **k**–**t** Are the same as (**a**–**j**), respectively, except they are for the November–December seasonal average. Purple stippling denotes values significant at the 90% level of confidence

seasonal average are opposite. For the Kenyan coastal plain and highlands west of Lake Victoria, the anomalies are not found to be significant for the transition period, but are so for the seasonal average.

5 Summary and conclusions

The seasonal cycle of the large-scale circulation over East Africa features a reversal of the cross-equatorial meridional

flow, from southerly in boreal summer to northerly in boreal winter. During boreal spring and fall, when rainfall is strongest, the circulation is in transition and the meridional flow is weak for a period of time during the season. Here we analyze multiple high-resolution atmospheric reanalyses and rainfall observations to improve our understanding of how interannual variations in the boreal spring and fall East African rains are associated with interannual variations in the transition periods of the cross-equatorial flow.

Spring and fall transition period start date, end date, and length are quantified using two daily time series of the 925-hPa meridional wind speed averaged between 40° E and 50° E on the equator formulated from four different atmospheric reanalysis. This location (925 hPa and 40° E–50° E) captures the low-level cross-equatorial meridional flow maximum. One time series is the raw data, while the other is linearly detrended and smoothed using a 30-day running mean filter to remove multi-decadal and sub-seasonal variations. As described in Sect. 3.2, start and end dates are identified for each season and each year in the detrended and smoothed daily time series of each reanalyses by utilizing the raw daily time series to select a threshold when the averaged 925-hPa meridional wind speed on the equator is considered "weak" in the detrended and smooth time series. The "weak" wind speed thresholds from the four reanalyses are averaged together to obtain a single threshold that is applied to all reanalyses to determine start date, end date, and transition period length.

In the climatology, the boreal spring transition period begins around March 3rd and lasts until April 3rd (32 days). During this period, 15–30% of the annual rainfall occurs over eastern Tanzania and the Turkana Channel of Kenya (Fig. 4). The beginning of the spring transition period, the low-level meridional height gradient over the southwestern Indian Ocean between 6° S and 15° S (Fig. 2) reverses and the zonal component of the low-level flow changes from westerly to easterly. These changes are associated with the seasonal weakening of the South Indian convergence zone (SICZ) that extends southeastward from the southeastern African coast over the Mozambique Channel and Madagascar. The end of the spring transition period is associated with the a reversal of the zonal low-level height gradient from positive to negative south of 2° S as the Mascarene High extends westward, and a reversal of the low-level meridional height gradient over the Arabian Sea.

The boreal fall transition period is one week shorter than the spring transition period, beginning on November 9th in the climatology and lasting until December 3rd (25 days). 20–40% of the total annual rainfall falls over the Kenyan coastal plains and southwestern Somalia (Fig. 4) during this time. The beginning of the fall transition is associated with a reversal of the low-level meridional height gradient over the Arabian Sea combined with a reversal from negative to positive of the low-level zonal height gradient north of 2° S, while the end of the period is marked by a reversal of the low-level zonal gradient north of 10° S. These changes represent a seasonal weakening of coastal ridging south of the equator as the Mascarene High weakens west of 70° E.

To understand how the length of the transition periods is determined, six types of events are defined. Short transition periods occur when an early beginning is dominated by an early end (SEE type), when a late beginning is accompanied by an early end (SLE), or when a late beginning dominates over a late end (SLL). Similarly, long transition periods are classified a LEE, LLE, or LLL. Only years in which 3 of the 4 atmospheric reanalyses agree are included. Composites for each reanalysis are formed by averaging cases, but only when there are at least 5 cases.

For the spring transition period, the SLE and LEL types are most common. The early start in the LEL case is associated with an early breakdown of the SICZ over the Mozambique Channel in association with an anomalously weak Mascarene High and strong ridging over the Arabian Sea (Fig. 8). These features are related to warm SSTAs in the western Indian Ocean that enhance low-level atmospheric moisture and convection over East Africa (Fig. 9) despite the little change in the onshore low-level easterly flow. The SLE has opposite anomalies.

In the boreal fall transition period, LEL, LLL, SEE, and SLE events are most common, and results indicate that they are also associated with variability of the Arabian and Mascarene Highs. Late start dates in LLL and SLE are both associated with weaker low-level northeasterlies due to higher heights in the western equatorial Indian Ocean for LLL and lower height over the Arabian Sea (Fig. 13b and c). Meanwhile the early start of LEL is associated with the opposite anomalous height pattern (Fig. 13a). The early start of SEE is different, as it is associated with a pattern of basin-wide weakening of the low-level heights and early development of the SICZ over the Mozambique Channel (Fig. 13d). The late end in LEL and LLL (Fig. 13e–f) are associated with a stronger Mascarene High over the southwestern Indian Ocean, while the early end in SEE is associated with the opposite response (Fig. 13h). The early end in SLE is associated with higher heights in the western equatorial Indian Ocean (Fig. 13g). It is the interaction between these high-pressure systems as the transition period evolves that helps to explain the differences in the associated rainfall anomalies over East Africa during the boreal fall transition period (Fig. 14).

From our results the following conclusions are drawn. They include:

- Our results above highlight the relative importance of the evolution of the SICZ/MCT and the Mascarene High in the southwestern Indian Ocean, and low-level

ridging over the Arabian Sea as they relate towards defining the boreal spring and fall transition period length over East Africa. Variations in the timing and/or intensity of these mechanisms can alter the low-level circulation patterns, wind convergence, atmospheric moisture content, and rainfall over East Africa. This suggests that accounting for such circulation mechanisms may offer some hope toward the improvement of East Africa rainfall prediction during the transition periods.

- Our results suggest that there may be some value using the transition period variability to predict seasonal rainfall anomalies over East Africa for the spring long rains and fall short rains. Our findings show general agreement between the transition period and the seasonal rainfall anomalies over East Africa for the LEL and SLE event types in the spring and fall (Figs. 9 and 15). Given that the transition period is only the beginning part of the longer boreal spring and fall seasons over East Africa, suggests that knowledge of the transition period variability may be informative for seasonal rainfall prediction in some instances such as during LEL and SLE events. For other event types, such as LLL and SEE during the boreal fall, knowledge of transition period variability may only provide limited regional value for prediction. The next step is to investigate using knowledge of transition period variability to predict East African seasonal rainfall variability.
- Air/sea coupling over the western Indian Ocean appears to be stronger during the spring transition period compared to the fall at interannual timescales. Based on our composite results for LEL and SLE, the East African rainfall anomalies (Fig. 9) are largely due to modifications through specific humidity (Fig. 10e–h) rather than a change in the low-level circulation, hence wind convergence (Fig. 8) for the spring transition period. Furthermore, the changes in low-level atmospheric moisture are directly associated with SSTAs over the western Indian Ocean during the spring transition period (Fig. 10a–d). This is in contrast to the fall transition period, where the rainfall anomalies appear to be primarily controlled by circulation variations (Fig. 13). This suggests that western Indian Ocean SSTAs may be a more useful predictor for the spring transition period rainfall anomalies over East Africa at interannual timescales, but the same may not the case for the fall transition period. Exactly why the spring and fall behave differently remains unclear. It is possible that remote forcing mechanisms, such as ENSO, play a more influential role in the fall transition period resulting in the disconnect in western Indian Ocean air/sea coupling as it relates to East African rainfall variability during this time of the year. More work is still needed to better understand this difference, and to evaluate using western Indian Ocean SSTs as a predictor for interannual rainfall variability during the boreal spring.

Model projections suggest that East African rainfall is likely to significantly change in the future with, in particular, increases in boreal fall precipitation (Cook and Vizy 2013; Rowell et al. 2015; Dunning et al. 2018; Dosio et al. 2019; Han et al. 2019). The understanding of the mechanisms that influence East African transition period variability on interannual timescales developed in this paper can potentially inform the analysis on multi-decadal timescales, with implications for climate prediction. This study highlights the relationship between the seasonal evolution low-level circulation features, namely the Mascarene High and Arabian High, and East African rainfall variability at interannual timescales. As our climate continues to warm, how these influential circulation features seasonally evolve will likely change, hence affecting the rainfall over this region in the future. Thus, results from this study may provide a contemporary understanding of the important physical processes associated with this relationship at shorter timescales that can help inform, and be used to assess the plausibility of future climate projections over East Africa. Of course, the next step is to first evaluate this relationship at decadal to multidecadal timescales to better understand how the processes identified at interannual timescales relate to longer-term changes of the climate system.

Acknowledgements This work was funded by NSF Award #1701520. The authors acknowledge the Texas Advanced Computing Center (TACC) at The University of Texas at Austin for providing HPC and database resources that have contributed these research results URL: https://www.tacc.utexas.edu. The Grid Analysis and Display System software (GrADS) developed at COLA/IGES was used for generating the figures.

References

Anyamba EK, Ogallo LJ (1985) Anomalies in the wind field over East Africa during the East African rainy season of 1983/1984. In: Proceedings of the first WMO workshop on diagnosis and prediction of monthly and seasonal atmospheric variations over the globe, long-range forecasting report series No 6 v1 WMO/TD. No 87: pp 128–133.

Ayugi BO, Wen W, Chepkemoi D (2016) Analysis of spatial and temporal patterns of rainfall variations over Kenya. J Environ Earth Sci 6:69–83

Ayugi BO, Tan G, Ongoma V, Mafuru KB (2018) Circulations associated with variations in boreal spring rainfall over Kenya. Earth Syst Environ 2:421. https://doi.org/10.1007/s41748-018-0074-6

Barimalala R, Desbiolles F, Blamey RC, Reason C (2018) Madagascar influence on the South Indian Ocean Convergence Zone, the Mozambique Channel Trough and southern African rainfall. Geophys Res Lett 45:11380–11389. https://doi.org/10.1029/2018GL079964

Black E, Slingo J, Sperber KR (2003) An observational study of the relationship between excessively strong short rains in coastal East

Africa and Indian Ocean SST. Mon Weather Rev 131:74–94. https://doi.org/10.1175/1520-0493(2003)131%3c0074:AOSOTR%3e2.0.CO;2

Cadet D, Desbois M (1981) A case study of a fluctuation of the Somali Jet during the Indian summer monsoon. Mon Weather Rev 109:182–187. https://doi.org/10.1175/1520-0493(1981)109%3c0182:ACSOAF%3e2.0.CO;2

Camberlin P, Okoola RE (2003) The onset and cessation of the "long rains" in eastern Africa and their interannual variability. Theor Appl Climatol 75:43–54. https://doi.org/10.1007/s00704-002-0721-5

Camberlin P, Philippon N (2002) The East African March–May rainy season: associated atmospheric dynamics and predictability over the 1968–97 period. J Clim 15:1002–1019. https://doi.org/10.1175/1520-0442(2002)015%3c1002:TEAMMR%3e2.0.CO;2

Clarke CO, Webster PJ, Cole JE (2003) Interdecadal variability of the relationship between the Indian Ocean zonal mode and East African coastal rainfall anomalies. J Clim 16:548–554. https://doi.org/10.1175/1520-0442(2003)016%3c0548:IVOTRB%3e2.0.CO;2

Cook KH (2000) The South Indian Convergence Zone and interannual rainfall variability over Southern Africa. J Clim 13:3789–3804. https://doi.org/10.1175/1520-0442(2000)013%3c3789:TSICZA%3e2.0.CO;2

Cook KH, Vizy EK (2013) Projected changes in East African rainy seasons. J Clim 26:5931–5948. https://doi.org/10.1175/JCLI-D-12-00455.1

Cook KH, Vizy EK (2019) Contemporary climate change of the African monsoon systems. Curr Clim Change Rep 5:145–159. https://doi.org/10.1007/s40641-019-00130-1

Copernicus Climate Change Service (C3S) (2017) ERA5: Fifth generation of ECMWF atmospheric reanalyses of the global climate. Copernicus Climate change Service Climate Data Store (CDS). https://cds.climate.copernicus.edu/cdsapp#!/home. Accessed 20 Apr 2019

Crossett CC, Metz ND (2017) A climatological study of extreme cold surges along the African Highlands. J Appl Meteorol Climatol 56:1731–1738. https://doi.org/10.1175/JAMC-D-15-0191.1

Dee DP, Uppala SM, Simmons AJ et al (2011) The ERA-Interim reanalysis: configuration and performance of the data assimilation system. Q J R Meteorol Soc 137:553–597. https://doi.org/10.1002/qj.828

Dosio A, Jones RG, Jack C, Lennard C, Nikulin G, Hewitson B (2019) What do we know about future precipitation in Africa? Robustness, significance and added value of projections from a large ensemble of regional climate models. Clim Dyn. https://doi.org/10.1007/s00382-019-04900-3

Dunning CM, Black E, Allan RP (2018) Later wet seasons with more intense rainfall over Africa under future climate change. J Clim 31:9719–9738. https://doi.org/10.1175/JCLI-D-18-0102.1

Fauchereau N, Trzaska S, Ricarhd Y, Roucou P, Camberlin P (2003) Sea-surface temperature co-variability in the southern Atlantic and Indian Oceans and its connections with atmospheric circulation in the Southern Hemisphere. Int J Climatol 23:663–677. https://doi.org/10.1002/joc.905

FEWSNET (2018) Alert: heavy rainfall and further flooding expected across East Africa through the end of May. FEWSNET Alert. https://fews.net/east-africa/alert/may-11-2018. Accessed 1 May 2019

Findlater J (1969) A major low-level air current near the Indian Ocean during the northern summer. Q J R Meteorol Soc 95:362–380. https://doi.org/10.1002/qj.49709540409

Funk C, Senay G, Asfaw A, Verdin J, Rowland J, Michaelson J, Eilerts G, Korecha D, Dhoularton R (2005) Recent drought tendencies in Ethiopia and equatorial-subtropical Africa. US Agency for International Development, Washington

Funk C, Dettinger MD, Michaelsen JC, Verdin JP, Brown ME, Barlow M, Hoell A (2008) Warming of the Indian Ocean threatens eastern and southern African food security by could be mitigated by agricultural development. Proc Natl Acad Sci USA 105:11081–11086. https://doi.org/10.1073/pnas.0708196105

Funk C, Husak G, Michaelsen J, Shukla S, Hoell A, Lyon B, Hoerling MP, Liebmann B, Zhang T, Verdin J, Galu G, Eilerts G, Rowland J (2013) Attribution of 2012 and 2003–12 rainfall deficits in eastern Kenya and southern Somalia. Bull Am Meteorol Soc 94:45–48

Funk C, Peterson P, Landsfeld M, Pedreros D, Verdin J, Shukla S, Husak G, Rowland J, Harrison L, Hoell A, Michaelsen J (2015) The climate hazards infrared precipitation with stations—a new environmental record for monitoring extremes. Sci Data 2:150066. https://doi.org/10.1038/sdata.2015.66

Gelaro R, McCarty W et al (2017) The modern-era retrospective analysis for research and applications, version 2 (MERRA-2). J Clim 30:5149–5454. https://doi.org/10.1175/JCLI-D-16-0758.1

Griffiths JF (1972) Eastern Africa. World survey of climatology, climates of Africa, vol 10. Elsevier, Amsterdam, pp 313–348

Han F, Cook KH, Vizy EK (2019) Changes in intense rainfall events and drought across Africa in the 21st century. Clim Dyn 53:2757–2777. https://doi.org/10.1007/s00382-019-04653-z

Hastenrath S, Polzin D, Mutai C (2011) Circulation mechanisms of Kenya rainfall anomalies. J Clim 24:404–412. https://doi.org/10.1175/2010JCLI3599.1

Hermes JC, Reason CJC (2005) Ocean model diagnosis of interannual coevolving SST variability in the south Indian and south Atlantic oceans. J Clim 18:2864–2882. https://doi.org/10.1175/JCLI3422.1

Indeje M, Semazzi FHM, Xie L (2001) Mechanistic model simulations of the East African climate using NCAR regional climate model: Influence of large-scale orography on the Turkana low-level jet. J Clim 14:2710–2724. https://doi.org/10.1175/1520-0442(2001)014%3c2710:MMSOTE%3e2.0.CO;2

Ishii M, Shouji A, Sugimoto S, Matsumoto T (2005) Objective analyses of sea-surface temperature and marine meteorological variables for the 20th century using ICOADS and the KOBE collection. Int J Climatol 25:865–879. https://doi.org/10.1002/joc.1169

Kobayashi S, Ota Y, Harada Y, Ebita A, Moriya M, Onoda H, Onogi K, Kamahori H, Kobayashi C, Endo H, Miyaoka K, Takahashi K (2015) The JRA-55 reanalysis: general specifications and basic characteristics. J Meteorol Soc Jpn 93:5–48. https://doi.org/10.2151/jmsj.2015-001

Krishnamurti TN, Bhalme HN (1976) Oscillations of a monsoon system. Part I. Observational aspects. J Atmos Sci 33:1937–1954. https://doi.org/10.1175/1520-0469(1976)033%3c1937:OOAMSP%3e2.0.CO;2

Krishnamurti TN, Molinari J, Pan H-L (1976) Numerical simulation of the Somali Jet. J Atmos Sci 33:2350–2362. https://doi.org/10.1175/1520-0469(1976)033%3c2350:NSOTSJ%3e2.0.CO;2

Lashkari H, Matkan AA, Mohammadi Z (2016) Local time changes over a 66-year period and annual relocation of Saudi Arabian subtropical high pressure. Open J Geol 6:1080–1095. https://doi.org/10.4236/ojg.2016.69081

Levin NE, Zipser EJ, Cerling TE (2009) Isotopic composition of waters from Ethiopia and Kenya: insights into moisture sources for eastern Africa. J Geophys Res 114:D23306. https://doi.org/10.1029/2009JD012166

Liebmann B, Hoerling MP, Funk C, Bladé I, Dole RM, Allured D, Quan X, Pegion P, Eischeid JK (2014) Understanding recent eastern Horn of Africa rainfall variability and change. J Clim 27:8630–8645. https://doi.org/10.1175/JCLI-D-13-00714.1

Liu W, Cook KH, Vizy EK (2020) Influence of Indian Ocean SSTs on the East African short rains. Clim Dyn **(submitted)**

Lyon B, DeWitt DG (2012) A recent and abrupt decline in the East African long rains. Geophys Res Lett 39:L02702. https://doi.org/10.1029/2011GL050337

Maidment RI, Allan RP, Black E (2015) Recent observed and simulated changes in precipitation over Africa. Geophys Res Lett 42:8155–8164. https://doi.org/10.1002/2015GL065765

Manatsa D, Behera SK (2014) On the major shifts in the IOD during the last century, the role of the Mascarene High displacements. Int J Climatol 34:2033–2046. https://doi.org/10.1002/joc.3820

Manatsa D, Morioka Y, Behera SK, Matarira CH, Yamagata T (2014) Impact of Mascarene high variability on the East African 'short rains'. Clim Dyn 42:1259–1274. https://doi.org/10.1007/s00382-013-1848-z

Manatsa D, Mudavanhu C, Mushore TD, Mavhura E (2016) Linking major shifts in East Africa 'short rains' to the Southern Annular Mode. Int J Climatol 36:1590–1599. https://doi.org/10.1002/joc.4442

McClanahan TR (1988) Seasonality in East Africa's coastal waters. Mar Ecol Prog Ser 44:191–199

Mekonnen A, Thorncroft CD (2016) On mechanisms that determine synoptic time scale convection over East Africa. Int J Climatol 36:4045–4057. https://doi.org/10.1002/joc.4614

Mekonnen A, Thorncroft CD, Aiyyer AR, Kiladis G (2008) Convectively coupled Kelvin waves over tropical Africa during the boreal summer: structure and variability. J Clim 21:6649–6667. https://doi.org/10.1175/2008JCLI2008.1

Metz ND, Archambault HM, Srock AF, Galarneau TJ Jr, Bosart LF (2013) A comparison of South American and African preferential pathways for extreme cold events. Mon Weather Rev 141:2066–2086. https://doi.org/10.1175/MWR-D-12-00202.1

Morioka Y, Takaya K, Behera SK, Masumoto Y (2015) Local SST impacts on summertime Mascarene high variability. J Clim 28:678–694. https://doi.org/10.1175/JCLI-D-14-00133.1

Munday C, Washington R (2017) Circulation controls on southern African precipitation in coupled models: the role of the Angola low. J Geophys Res Atmos 122:861–877. https://doi.org/10.1002/2016JD025736

Mutai CC, Ward MN, Colman AW (1998) Towards the prediction of the East Africa short rains based on sea-surface temperature–atmosphere coupling. Int J Climatol 18:975–997. https://doi.org/10.1002/(SICI)1097-0088(199807)18:9%3c975:AID-JOC259%3e3.0.CO;2-U

Nicholson SE (1996) A review of climate dynamics and climate variability in eastern Africa. In: Johnson TC, Odada EO (eds) The limnology, climatology, and paleoclimatology of the East African Lakes. Gordon and Breach Publ, Amsterdam, pp 25–56

Nicholson SE (2016) Short communication: an analysis of recent rainfall conditions in eastern Africa. Int J Climatol 36:526–532. https://doi.org/10.1002/joc.4358

Nicholson SE (2017) Climate and climatic variability of rainfall over eastern Africa. Rev Geophys 55:590–635. https://doi.org/10.1002/2016RG000544

Nicholson SE, Selato JC (2000) The influence of La Nina on African rainfall. Int J Climatol 20:1761–1776. https://doi.org/10.1002/1097-0088(20001130)20:14%3c1761:AID-JOC580%3e3.0.CO;2-W

Nigam T, Pant V, Ravi Prakash K (2018) Impact of Indian Ocean dipole on the coastal upwelling features off the southwest coast of India. Ocean Dyn. https://doi.org/10.1007/s10236-018-1152-x

Novella NS, Thiaw WM (2013) African rainfall climatology version 2 for famine early warning systems. J Appl Meteorol Climatol 52:588–606

Ogallo LA (1993) Dynamics of the East African climate. Proc Indian Acad Sci 102:203–217. https://doi.org/10.1007/BF02839191

Ogwang A, Ongoma V, Xing L, Ogou FK (2015) Influence of Mascarene high and Indian Ocean dipole on East African extreme weather events. Geographica Pannonica 19:64–72. https://doi.org/10.5937/geopan1502064o

Ongoma V, Chen H (2017) Temporal and spatial variability of temperature and precipitation over East Africa from 1951 to 2010. Meteorol Atmos Phys 129:131–144. https://doi.org/10.1007/s00703-016-0462-0

Owiti Z, Ogallo LA, Mutemi J (2008) Linkages between Indian Ocean dipole and East African seasonal rainfall anomalies. J Kenya Meteorol Soc 2:3–17

Pant GB, Kumar KR (1997) Climates of South Asia. Wiley, Hoboken, p 320

Raju PVS, Bhatla R (2014) Evolution of withdrawal features of the southwest monsoon over India. Int J Climatol 34:1860–1872. https://doi.org/10.1002/joc.3806

Ramage CS (1971) Monsoon meteorology. Academic Press, Cambridge, p 296

Riddle EE, Cook KH (2008) Abrupt transitions over the greater Horn of Africa: observations and regional model simulations. J Geophys Res 113:D15109. https://doi.org/10.1029/2007JD009202

Rodwell MJ, Hoskins BJ (1995) A model of the Asian summer monsoon. Part II: cross-equatorial flow and PV behavior. J Atmos Sci 52:1341–1356

Rowell DP, Booth BBB, Nicholson SE, Good P (2015) Reconciling past and future rainfall trends over East Africa. J Clim 28:9768–9788. https://doi.org/10.1175/JCLI-D-15-0140.1

Sun L, Semazzi FHM, Giorgi F, Ogallo L (1999) Application of the NCAR regional climate model to eastern Africa 1. Simulation of the short rains of 1988. J Geophys Res 104:6529–6548. https://doi.org/10.1029/1998JD200051

Swallow JC, Schott F, Fieux M (1991) Structure and transport of the East African coastal current. J Geophys Res 96:22245–22257. https://doi.org/10.1029/91JC01942

Ummenhofer CC, Sen Gupta A, England MH, Reason CJC (2009) Contributions of Indian Ocean sea surface temperatures to enhanced East African rainfall. J Clim 22:993–1013. https://doi.org/10.1175/2008JCLI2493.1

Ummenhofer CC, Kulüke M, Tierney JE (2018) Extremes in East African hydroclimate and links to Indo-Pacific variability on interannual to decadal timescales. Clim Dyn 50:2971–2991. https://doi.org/10.1007/s00382-017-3786-7

Varela R, Alverez I, Santos F, deCastro M, Gomez-Gesteira M (2015) Has upwelling strengthened along worldwide coasts over 1982–2010? Nat Sci Rep 5:10016. https://doi.org/10.1038/srep10016

Vizy EK, Cook KH (2014) Impact of cold air surges on rainfall variability in the Sahel and wet African tropics: aA multi-scale analysis. Clim Dyn 43:1057–1081. https://doi.org/10.1007/s00382-013-1953-z

Vizy EK, Cook KH (2019) Observed relationship between the Turkana low-level jet and boreal summer convection. Clim Dyn. https://doi.org/10.1007/s00382-019-04769-2

Webster PJ, Magaña VO, Palmer TN, Shukla J, Tomas RA, Yanai M, Yasunari T (1998) Monsoons: processes, predictability, and the prospects for prediction. J Geophys Res 103:14451–14510. https://doi.org/10.1029/97JC02719

Williams AP, Funk C, Michaelsen J, Rauscher SA, Robertson I, Wils THG, Koprowski M, Eshetu Z, Loader NJ (2012) Recent summer precipitation trends in the Greater Horn of Africa and the emerging role of Indian Ocean sea surface temperature. Clim Dyn 39:2307–2328. https://doi.org/10.1007/s00382-011-1222-y

Wen-Jing S, Zi-Niu X (2014) Impact of the preceding boreal winter southern annular mode on the summertime Somali Jet. Atmos Oceanic Sci Lett 7:534–539. https://doi.org/10.3878/AOSL20140045

Yang W, Seager R, Cane MA (2015) The annual cycle of East African precipitation. J Clim 28:2385–2404. https://doi.org/10.1175/JCLI-D-14-00484.1